Enhancing Untethered Robot Localization: A Fusion Approach Integrating Magnetic Coupling Localization and Ultrasound Imaging

This thesis was written by **Deniz Alp Uğurlu**,
as part of the master **Mechanical Engineering**,
in the department of **Biomechanical Engineering**,
at the **University of Twente**.

November 2023
BE-971

The graduation committee comprises

Prof. Dr.-Ing. Jutta Arens	as	**Chair of the Committee**,
Dr. Islam S.M. Khalil	as	**Daily Supervisor**,
Dr. Janset Dasdemir	as	**Daily Supervisor**, and
Dr. Ir. Ronald G.K.M. Aarts	as	**External Assessor**.

CONTENTS

Abstract*—This study introduces a noninvasive localization approach aimed at fusing the data streams from slow-rate pulse-echo sensors and fast-rate magnetic coupling localization (MCL) sensors, to enhance the positioning precision of externally actuated untethered magnetic robots (UMRs). These systems work by robotically moving rotating permanent magnets (RPMs) enabling control of UMRs in bodily fluids for targeted therapy. By combining the position information of UMRs derived from MCL with the environment's reconstructed imagery acquired through ultrasound imaging, essential feedback details can be swiftly ascertained with reduced uncertainty. First, we demonstrate the capabilities and limitations of MCL on its own. Investigating down-scaling of the UMR shows us that the localization accuracy of a 12-mm UMR, an 8-mm UMR, a 5-mm UMR, and a 3-mm UMR at a distance of 180 mm from the RPM, in terms of the mean absolute position error, is 0.7 ± 0.7 mm, 0.9 ± 0.4 mm, 1.3 ± 0.2 mm, and 0.3 ± 0.1 mm, respectively. This error tends to decrease when lowering the actuation frequency of the UMR, particularly when operating above the zero dB crossing of the RPM actuator. Second, we formulate a model for directly fusing data from two sensors—specifically, MCL and ultrasound localization. Then we use this fused data to showcase the effective and complementary roles provided by the sensors in enhancing localization accuracy during the wireless actuation. The fusion mechanism empowers the localization of UMRs within blood vessel phantoms, enabling continuous feedback provision even in scenarios where ultrasound signals are obstructed, temporarily or permanently, by wave reflectors. Our findings emphasize that the mean absolute position error for an 8-mm UMR, positioned 140 mm away from the RPM actuator, during pulse-echo localization interruptions, averages 1.4 ± 0.3 mm ($n = 18$), considering 4 different simulated interruption patterns with 3 distinct measurements each.

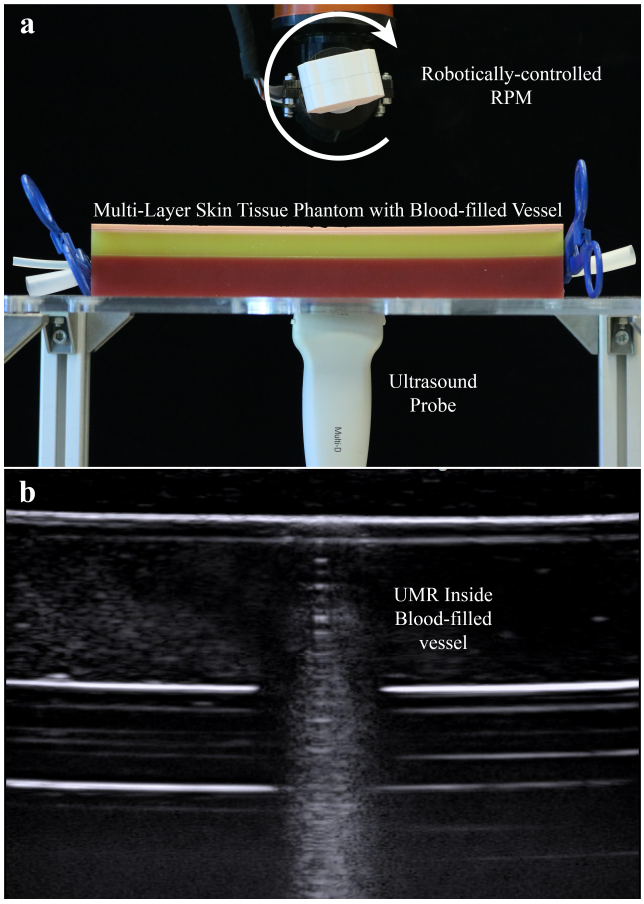

Fig. 1. An untethered magnetic robot (UMR) is maneuvered within a blood vessel phantom, and its position can be ascertained using either magnetic coupling or ultrasound images. (a) Magnetic coupling and ultrasound images are simultaneously estimated and measured. (b) The ultrasound image provides a clear longitudinal cross-section of the phantom, revealing a distinct silhouette of the UMR within the vessel. Combining ultrasound data with magnetic coupling localization data improves positioning accuracy.

I. Introduction

UNTETHED magnetic robots hold promise in diagnostics and targeted drug delivery by enabling interventions with minimal incisions and access to deep-seated-regions of the human body [1], [2], [3]. The key advantage of these untethered magnetic robots (UMRs) in biomedical applications has emerged when clinical imaging modalities, like ultrasound (US) systems, were incorporated with wireless manipulation systems to provide feedback and enable accurate *in vivo* tracking and control without visual inspection [4], [5]. On the fundamental side, this integration allowed us to study and understand the performance characteristics of a wide range of UMRs *in vivo*, where different flow patterns, near-wall effects, heterogeneous rheological properties, and concentrated cells are likely to affect the motion. Currently, UMRs can be systematically maneuvered from their initial insertion point to a predetermined target, and subsequently retrieved. Under the anticipated *in vivo* circumstances, the need for noninvasive localization becomes crucial for real-time control. It is essential that this localization requirement does not excessively complicate wireless manipulation systems by introducing a notable complexity due to the interplay between actuation and localization.

The integration of wireless magnetic manipulation and medical imaging systems has been achieved in several ways based on the working principle of wireless actuation and noninvasive localization [1], [6]. Typically, in state-of-the-art systems, the power, electronic, electromechanical, and localization systems required to control the UMRs are separated and/or embedded into wireless manipulation systems. This approach allows for simplifications to the design of UMRs into a wire formed into a helix or an elastic tail to achieve locomotion by transverse bending waves along their length [7], [8], or using rigid structures with simple geometric features (spherical, ellipsoidal, and cylindrical) [9]. Alternatively, propulsion is achieved by rolling or tumbling on a nearby solid boundary [10]. Although this approach enables the design of the UMRs to be simplified, the wireless manipulation systems become significantly more complex and hinder the transfer of this technology into *in vivo* applications for two key reasons. First, wireless actuation and noninvasive localization rely on the transduction of energy from the actuator magnet or electromagnet to the UMR to create work (i.e., mechanical energy in the form of locomotion or oscillation) and from the UMR to a transducer to create a detectable signal (i.e., needed for localization). These requirements place strict constraints on the actuation and localization systems in terms of their type and configuration. Second, the integration of existing noninvasive imaging systems is not straightforward because they are conceived to achieve specific

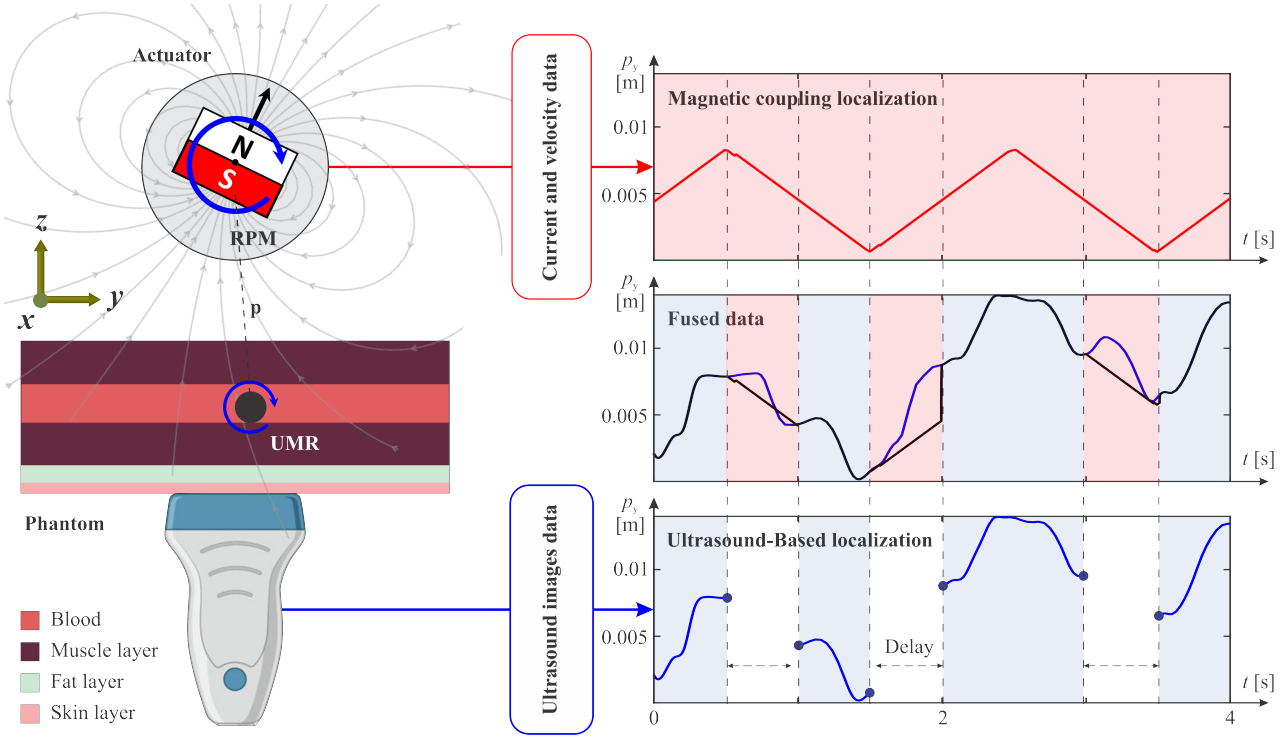

Fig. 2. The spherical UMR is rolled inside a blood vessel phantom with the RPM's position controlled to achieve straight runs along the y-axis. The current drawn by, and the angular velocity of the actuator are used to estimate the position of the UMR with respect to the RPM. The RPM is simultaneously localized using ultrasound images. Ultrasound scans are gathered at a rate of 20 Hz, while MCL estimates the position of the UMR at a rate of 167 Hz.

medical imaging operations. Consequently, the fusion process of wireless actuation and imaging systems is likely to impose physical constraints, limiting optimum performance, especially in cases where multiple actuators are required [11], [12]. Despite these limitations, there have been two approaches to tackle these issues. The first approach incorporates additional functionalities to the existing imaging system [13], [14], while the second introduces arrays of multiple sensors to measure the UMR's field [15]. Recently, there has been a rapid development in the first approach through the integration of non-invasive imaging systems (e.g., computed tomography [16], magnetic resonance [17], ultrasound [18], photoacoustic [19], electrical impedance tomography [20] and magnetic [21]) with magnetic manipulation systems. This integration has enabled implementing wireless actuation and motion control experiments in conditions similar to these encountered *in vivo*, or even realize wireless control *in vivo* [22], [23]. Niedert *et al*. conducted an operation involving a tumbling microrobot within an animal colon. This was achieved by utilizing an external time-periodic magnetic field in conjunction with an ultrasound imaging system [24], [25]. Vonthrom *et al.* have utilized a clinical magnetic resonance imaging (MRI) system to localize, steer, and control microrobots and microdevices [13]. Likewise, Tiryaki *et al*. demonstrated the efficacy of an MRI-powered magnetic miniature capsule robot. This innovative approach harnessed the acoustic streaming forces generated by high-intensity focused ultrasound to facilitate controlled drug release [14]. Servant *et al*. have used the feedback of an optical fluorescence imaging system to control a swarm of functionalized artificial bacterial flagella *in vivo* [26]. Pane *et al.* have presented a noninvasive localization strategy based on ultrasound acoustic phase analysis and demonstrated feedback control of a microrobot inside a tissue-mimicking phantom [27]. This principle of using the specific acoustic phase modulation produced by the motion of the microrobot has been implemented to enhance the contrast of the ultrasound images and enable robust feedback control.

In contrast to the use of imaging systems, the second approach relies on the utilization of magnetic field sensors either onboard the UMR or within a scalable workspace based on the configuration of the sensors. Popek *et al.* have demonstrated simultaneous localization and closed-loop propulsion of a capsule containing embedded Hall-effect sensors using a single rotating actuator magnet [28]. The incorporation of these sensors aboard such a capsule has proven to create a useful level of information even beyond localization. For example, Miller *et al.* have used Hall-effect sensors aboard a capsule to perceive the onset of step-out and adopt a strategy to keep the capsule in sync [29]. However, this method can be used to localize relatively large capsules since the field sensors and its wireless circuit should be integrated within its body, and is particularly useful when considering medical applications in the gastrointestinal system or inside natural lumen pathways with relatively large diameters. Alternatively, arrays (1-D, 2-D, and 3-D) of magnetic field sensors have been used to measure the magnetic field of UMRs and use the pre-calculated field of the actuator magnet to achieve localization [30]-[33]. Just recently, Zhang *et al*. have introduced a novel approach involving simultaneous magnetic localization and actuation. They have achieved this through an eye-in-hand

TABLE I

COMPARISON OF THE MAGNETIC COUPLING LOCALIZATION (MCL) WITH THE STATE-OF-THE-ART METHODS THAT HAVE BEEN USED IN THE FIELD OF SMALL-SCALE ROBOTICS [4]. OPTICAL TECHNIQUES ARE CLASSIFIED INTO REFLECTION AND FLUORESCENCE. ELECTRICAL IMPEDANCE TOMOGRAPHY (EIT) IS CLASSIFIED INTO CONVENTIONAL EIT AND MULTI-FREQUENCY EIT [43], [20]. THE SYMBOLS (+++) AND (- - -) REFLECT THE LEVEL OF GREATEST PROMISE AND DRAWBACK, RESPECTIVELY, FOR A GIVEN FEATURE (E.G., RESOLUTION OR BIOCOMPATIBILITY). THE ACRONYMS LOC AND EQ. INDICATE LOCALIZATION AND EQUIPMENT, RESPECTIVELY.

	Optical		Ultrasound		Radiation	EIT		Magnetic techniques			
Method	Reflection	Fluorescence	B-mode	Doppler	CT/X-rays	Conventional.	Multi-frequency	MRI	MPI	MFS	**MCL**
Temporal res.	+++	-	+++	++	++	-	-	- - -	++	NA	NA
Spatial res.	+++	-	++	++	++	- -	- -	+++	- -	NA	NA
Loc. speed	+	+	+	+	+	+	+	-	+	+	+++
Loc. depth	-	-	++	++	+++	-	-	+++	++	+	++
Biocompat.	+++	+	+++	+++	- - -	++	++	+	+	++	+++
Complexity	+	+++	+++	+++	-	+++	+++	+	++	-	+++
EQ. cost	-	- -	-	-	- - -	+	+	- -	- -	++	+++
Training req.	+	+	+	+	- - -	-	-	- - -	- -	+	+
EQ. size	+	+	+	+	- - -	+	+	- - -	- - -	+	+++

configuration for magnetic field sensors and a mobile electromagnetic manipulation system [34]. Notably, the challenge of Hall-effect sensor saturation can frequently be overcome by effectively choosing suitable sensors or by increasing the separation between the sensors and the actuator magnet.

In this study, we introduce and verify a non-invasive localization method for UMRs within fluid-filled lumens. This method works by estimating the permanent magnetic coupling between the magnetic moment of a rotating permanent magnet (RPM) actuator and a nearby UMR. The estimation of the magnetic coupling is achieved relying on the same signals that are used for actuation of the RPM (i.e., electric current and angular velocity), enabling simultaneous wireless actuation and localization *without* additional sensors. We demonstrate the validity of this magnetic coupling localization (MCL) method using magnetic roller ranging from 12 mm to 3 mm in diameter and investigate the influence of the actuation parameters on the localization error.

Our MCL differs from the conventional imaging techniques (Table I) that have been employed in the field of small-scale robotics [4] due to its ability to solely determine the position of a UMR through the estimation of magnetic torque. As we lack the capability to construct a 2-D or 3-D image of the environment, MCL must be integrated with a traditional imaging system using a hybrid approach. To ensure precise predictions, this hybrid technique would merge the estimated position from MCL with images reconstructed using one of the conventional methods. The integration of multiple data sources is pivotal to enhancing the robustness of localization.

It is noteworthy that optical, pulse-echo, ionizing radiation, electrical impedance tomography, and magnetic-based imaging techniques leverage the same core principle—signal absorption and attenuation captured by detectors to create image patterns of tissue and natural pathways. When a UMR is placed within tissue or a natural pathway, it can be detected through these same image patterns. Nevertheless, maintaining sufficient frame rates for transmitted images is imperative. Consequently, localization would need to be executed at an accelerated pace, ensuring that the UMR's position is promptly determined and used in feedback control. Alternatively, if images collected from an imaging system are employed to reconstruct the surroundings' interior, MCL can then ascertain the UMR's location. This leads to an increased localization speed, rendering wireless closed-loop control more attainable. This is one of the advantages inherent to MCL as compared to traditional imaging techniques.

Table I shows a comparison between the traditional imaging techniques and MCL. Using Hall-effect sensors or MCL to track UMRs requires that the physical surroundings be reconstructed. However, MCL does not require any sensors aboard the UMR or within its workspace. Therefore, it is economically advantageous to track a UMR using MCL (over Hall-effect methods) regardless of the temporal and spatial resolution of the imaging system, which is required to reconstruct the physical surroundings. MCL provides a direct way to determine the position without the need for image reconstruction. Therefore, it is reasonable to expect the localization speed of MCL to be greater than that of any other traditional method. Because of the transparency of the human body to magnetic fields, magnetic techniques (including MCL) have greater localization depth than any other method except for radiation methods.

This thesis presents such a hybrid noninvasive localization approach that fuses data acquired from ultrasound images and magnetic coupling localization (MCL). While ultrasound imaging has demonstrated its capability to provide localization, the presence of wave reflectors *in vivo* is likely to negatively impact the quality of collected data. Through the fusion of MCL with ultrasound image data, we introduce a localization method that surpasses conventional approaches. From a practical standpoint, exploiting the rapid-rate encoder feedback, and determining the UMR's position from the RPM actuator sensors offers a computational advantage. Additionally, It is important to note that due to the human body's magnetic field transparency, achieving the UMR's position through MCL offers distinct physical benefits.

We demonstrate our localization outcomes through the control of a UMR (i.e., milli-roller) within a blood vessel phantom, filled with porcine blood, utilizing a position-controlled RPM. This RPM is controlled by a 6-degrees-of-freedom (DOF) manipulator (Fig. 1(a)), facilitating adjustment of the RPM-UMR gap. While in motion inside the blood vessel

phantom, ultrasound images are gathered to reconstruct the internal structure of the phantom, encompassing layers such as skin, fat, muscle, and lumen, as shown in Fig. 1(b).

The thesis is organized as follows: Section II provides mathematical modeling and numerical results of the permanent magnetic coupling between the RPM actuator and the UMR. In addition, the model is used to investigate the trade-offs between localization and motion control. Estimation of the magnetic coupling using the inputs and states of the actuator RPM is presented in Section III for various actuation performances (e.g., actuation and translational speed of the RPM). In Section IV, we discuss experimental results to illustrate the simultaneous actuation and localization of a UMR inside a fluid-filled lumen using an RPM fixed to the end-effector of a robotic manipulator. In Section V, we elaborate on the implementation of localization using MCL and ultrasound images, outlining the limitations inherent in each technique. Furthermore, we present our devised data fusion strategy. Section VI introduces a performance evaluation framework designed to assess the effectiveness of both traditional ultrasound localization and sensor fusion localization solutions. Discussions pertaining to the practical limitations of our MCL method, the fusion of localization methods, and a comparison with state-of-the-art localization techniques are provided in Section VII. Finally, Section VIII concludes the thesis and provides direction for future work.

II. Magnetic Coupling Between an RPM and a UMR

Magnetic coupling between an RPM and a UMR (e.g., tumbling robot, helix, roller, ellipsoid) enables them to be oriented in synchrony [35]. In what follows, we discuss the theoretical background behind the interactions between an RPM and a UMR to determine the magnetic coupling from the signals that are used to actuate the RPM. In this thesis, the symbol $\hat{}$ denotes an estimation of a variable (e.g., $\hat{\mathbf{p}}$ is the estimated position of the UMR). Unit-length vectors are denoted by Blackboard bold (e.g., $\mathbb{m}$ denotes the unit-length magnetic moment of the UMR).

A. Magnetic Interactions

We consider a UMR of magnetic dipole moment $\mathbf{m} \in \mathbb{R}^3$, actuated using an RPM with a magnetic dipole moment $\mathbf{M} \in \mathbb{R}^3$. The UMR and RPM locations are characterized by the position vectors ${}^{O}\mathbf{p}_{\mathrm{rob}} \in \mathbb{R}^3$, positioned in the center of the UMR, and ${}^{O}\mathbf{p}_{\mathrm{act}} \in \mathbb{R}^3$, positioned in the center of the RPM, with respect to a reference frame, respectively (Fig. 2). The interaction between the two dipoles depends on their relative position vector, $\mathbf{p} = {}^{O}\mathbf{p}_{\mathrm{rob}} - {}^{O}\mathbf{p}_{\mathrm{act}}$, and the magnitude of their respective dipole moments. When the UMR is placed in the vicinity of the RPM's generated magnetic dipole field, $\mathbf{B}(\mathbf{p}, \mathbb{M})$, it experiences a magnetic force, $\mathbf{f}_{\mathrm{m}} = (\mathbf{m} \cdot \nabla)\mathbf{B}(\mathbf{p}, \mathbb{M})$, and magnetic torque, $\mathbf{T}_{\mathrm{m}} = \mathbf{m} \times \mathbf{B}(\mathbf{p}, \mathbb{M})$, which can be further expressed as

$$\mathbf{f}_{\mathrm{m}} = \frac{3\mu_0 \|\mathbf{M}\| \|\mathbf{m}\|}{4\pi \|\mathbf{p}\|^4} \left(\mathbb{M}\mathbb{m}^T + \mathbb{m}\mathbb{M}^T + (\mathbb{m}^T \mathbf{Z} \mathbb{M})\mathbf{I} \right) \mathbb{p}, \quad (1)$$

where $\mu_0 = 4\pi \times 10^{-7}$ N.A^{-2} is the permeability of free space and $\mathbf{Z} = \mathbf{I} - 5\mathbb{p}\mathbb{p}^T$. Similarly, the magnetic torque is given by

$$\mathbf{T}_{\mathrm{m}} = \frac{\mu_0 \|\mathbf{M}\| \|\mathbf{m}\|}{4\pi \|\mathbf{p}\|^3} \mathbb{m} \times \mathbf{D}(\mathbb{p}) \mathbb{M}, \quad (2)$$

where $\mathbf{D}(\mathbb{p}) = 3\mathbb{p}\mathbb{p}^T - \mathbf{I}$, and $\mathbf{I} \in \mathbb{R}^{3\times3}$ is the identity matrix [36]. The magnetic torque aligns the UMR's dipole moment with the applied field, while the magnetic force pulls the UMR in the direction determined by the field's spatial derivative and the UMR's dipole moment. Fig. 2 shows the roto-translational motion of the UMR, when the RPM's rotation, $\boldsymbol{\Omega}_{\mathrm{act}}$, is perpendicular to the axis of the lumen. Similarly, the UMR produces its magnetic field, which affects the RPM. This effect is necessarily limited by the distance between the RPM and the UMR, and the magnetic dipole moment of the UMR, as shown in Fig. 3. The magnetic field spatial gradient produced by the UMR's dipole moment will cause the RPM to experience a force $\mathbf{f}_{\mathrm{M}} = (\mathbf{M} \cdot \nabla)\mathbf{B}(\mathbf{p}, \mathbb{m})$, that scales as $\|\mathbf{f}_{\mathrm{M}}\| \sim \|\mathbf{M}\| \|\mathbf{m}\| \|\mathbf{p}\|^{-4}$, as shown in Fig. 3(a). The force $\mathbf{f}_{\mathrm{M}}$ produces a torque which will cause the RPM to rotate about its rotation axis, $\boldsymbol{\Omega}_{\mathrm{act}}$. This force is given by

$$\mathbf{f}_{\mathrm{M}} = \frac{3\mu_0 \|\mathbf{M}\| \|\mathbf{m}\|}{4\pi \|\mathbf{p}\|^4} \left(\mathbb{m}\mathbb{M}^T + \mathbb{M}\mathbb{m}^T + (\mathbb{M}^T \mathbf{Z} \mathbb{m})\mathbf{I} \right) \mathbb{p}. \quad (3)$$

Due to the UMR's rotation about the axis $\boldsymbol{\omega}_{\mathrm{rob}}$, a torque $\mathbf{T}_{\mathrm{M}} = \mathbf{M} \times \mathbf{B}(\mathbf{p}, \mathbb{m})$ will be generated on the RPM to align its magnetic moment with its own oscillating magnetic field such that

$$\mathbf{T}_{\mathrm{M}} = \frac{\mu_0 \|\mathbf{M}\| \|\mathbf{m}\|}{4\pi \|\mathbf{p}\|^3} \mathbb{M} \times \mathbf{D}(\mathbb{p}) \mathbb{m}. \quad (4)$$

This magnetic torque scales as $\|\mathbf{T}_{\mathrm{M}}\| \sim \|\mathbf{M}\| \|\mathbf{m}\| \|\mathbf{p}\|^{-3}$ (Fig. 3(b)), and affects the rotational dynamics of the permanent magnet rotor of the electric motor that rotates the RPM. It is possible that the inertia of the RPM could be dominant over the torque that the UMR would generate on the RPM. In this specific case, the inertia of the RPM and the magnetic torque of the UMR can be adjusted to yield a detectable magnetic torque (Fig. 3). For a given UMR and RPM; at a given localization gap between them, the permanent magnetic coupling has to be maintained and its magnitude must be large enough and depend solely on the relative position $\mathbf{p}$. It is well known that the gradient (Fig. 3(c)) falls off with the localization gap between the RPM and the UMR inversely by one power greater than the field (Fig. 3(d)). This explains why our localization method can determine the magnetic coupling using the motor of the RPM, assuming that all of its nominal parameters are known a priori.

B. Permanent Magnetic Coupling

Developing a rotating field-generation system using permanent magnets typically requires an electric motor. In such a device, the electromagnetic stator surrounds a permanent magnet rotor that is rigidly connected to the RPM. The differential equation governing the mechanical system of the motor is given by

$$(J_1 + J_2)\frac{\mathrm{d}\Omega}{\mathrm{d}t} + T_{\mathrm{M}} = K_{\mathrm{t}} I_{\mathrm{a}}, \quad (5)$$

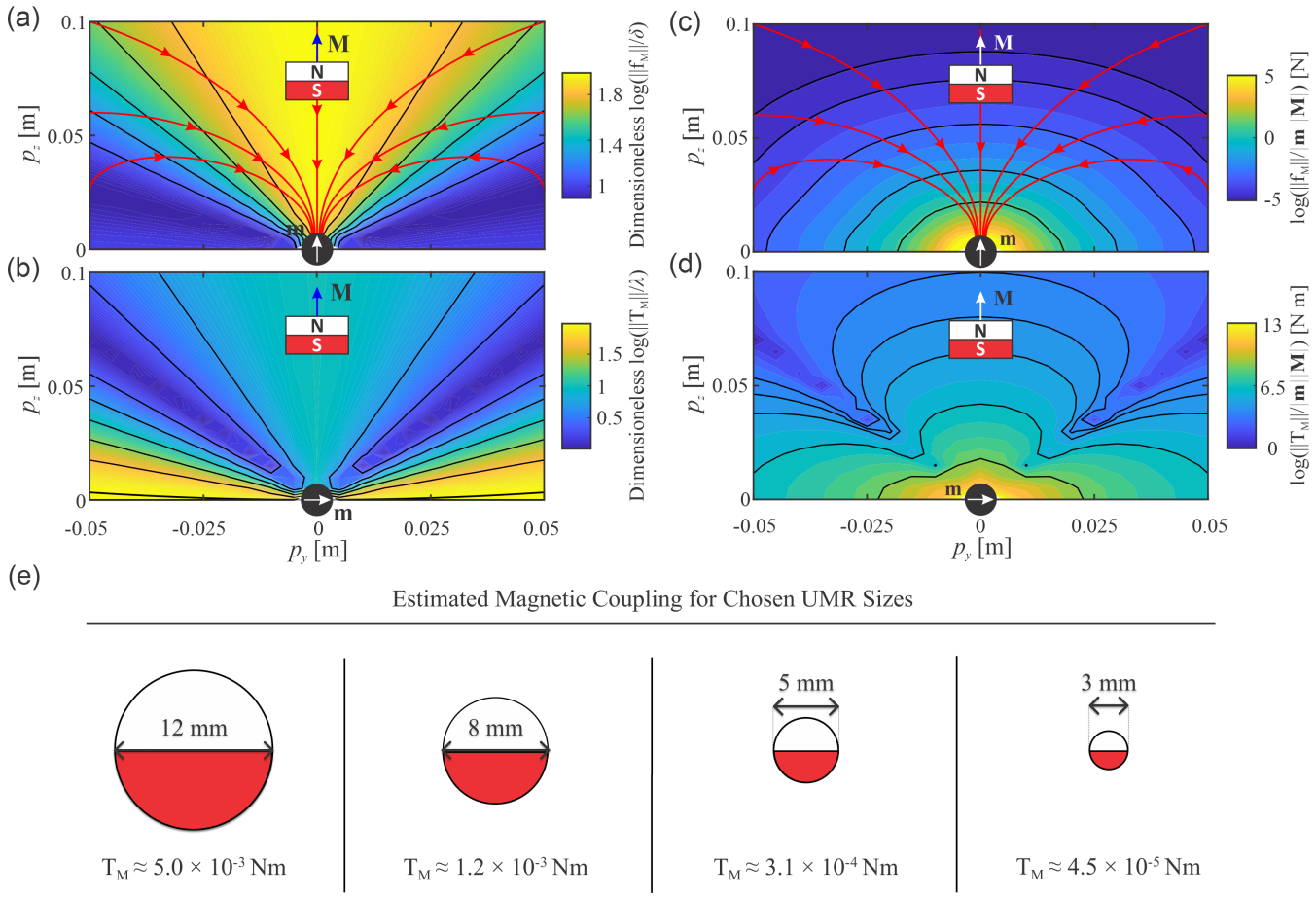

Fig. 3. Magnetic force, $\mathbf{f}_{\mathrm{M}}$, and torque, $\mathbf{T}_{\mathrm{M}}$, between an RPM with magnetic moment $\mathbf{M}$ and a UMR with magnetic moment $\mathbf{m}$ are nondimensionalized by $\delta = 3\mu_0\|\mathbf{M}\|\|\mathbf{m}\|/4\pi\|\mathbf{p}\|^4$ and $\lambda = \mu_0\|\mathbf{M}\|\|\mathbf{m}\|/4\pi\|\mathbf{p}\|^3$, respectively. a) Attractive magnetic force lines in red are calculated according to Equation (3), assuming the UMR's dipole moment $\mathbf{m}$ is aligned with the magnetic field produced by the RPM. The maximum attractive force is specified over an axial region between the RPM and the UMR. b) The dimensionless torque $\|\mathbf{T}_{\mathrm{M}}\|/\lambda$ is approximately 1 and can provide the smallest detectable torque if $\mathbf{m}$, $\mathbf{M}$, and $\mathbf{p}$ are known a priori. c) $\mathbf{f}_{\mathrm{M}}$ and $\mathbf{T}_{\mathrm{M}}$ are calculated and scaled by their moments $\mathbf{M}$ and $\mathbf{m}$, respectively. The magnetic force is expected to fall off approximately as p_z^{-4}. d) A magnetic coupling falls off approximately as p_z^{-3} and induces a back-emf which would counteract the applied voltage, that is used to actuate the RPM. e) Approximate values of magnetic coupling $\mathbf{T}_{\mathrm{M}}$ for different sizes of UMR and at various distances can be obtained from (b) using nominal values of the UMR (Table II and a localization gap of 75 mm.

where J_1 and J_2 represent the inertia of the permanent magnet rotor of the motor and the inertia of the RPM connected to the motor as a load, respectively. T_{M} is the external torque produced on the RPM due to a nearby UMR and any external torque. The total torque, $K_{\mathrm{t}}I_{\mathrm{a}}$, produced by the DC motor is determined by the flux and current. Since the flux is constant in this system, the torque is only proportional to the current I_{a}, where K_{t} is the torque constant. When an external torque is applied to the permanent magnetic rotor of the DC motor, its motion will induce a back electromotive force (emf) which would in turn counteract the applied voltage, changing the current drawn. A time-varying back-emf will be generated to counteract the changes in the total magnetic flux, ϕ, infringed on the loop of the actuator, such that $\varepsilon = \mathrm{d}\phi/\mathrm{d}t = K_{\mathrm{e}}\Omega(t)$, where k_{e} is the back-emf constant. With Equation (5), the back-emf closes the loop between the input voltage, $V(t)$, and the output angular velocity, $\Omega(t)$, as follows:

$$V(t) - \varepsilon(t) = L\frac{\mathrm{d}I_a}{\mathrm{d}t} + RI_a(t), \tag{6}$$

where L and R are the inductance and resistance, respectively, of the coils of the actuator. If the magnetic coupling between the UMR and the RPM is large enough such that we can sense its effect on the current drawn, then equations (5) and (6) can be used to determine the magnetic coupling. This magnetic coupling is fundamentally limited by the inertia of the RPM. MCL will likely demand an appropriate choice of RPM parameters for a given UMR. Note also that the angular velocity of the RPM typically requires a closed-loop control input. The closed-loop behavior of system (5) to the desired angular velocity, Ω_{des}, and the magnetic coupling input, T_{M}, is given by

$$\begin{aligned}\Omega = &\frac{C(s)E(s)G(s)}{1 + C(s)E(s)G(s) + k_{\mathrm{e}}E(s)G(s)}\Omega_{\mathrm{des}} \\ &+ \frac{G(s)}{1 + C(s)E(s)G(s) + k_{\mathrm{e}}E(s)G(s)}T_{\mathrm{M}},\end{aligned} \tag{7}$$

where $C(s)$, $E(s)$, and $G(s)$ are the transfer functions of the control, electrical, and mechanical systems of the DC motor, respectively (provided in Appendix A). If the angular velocity

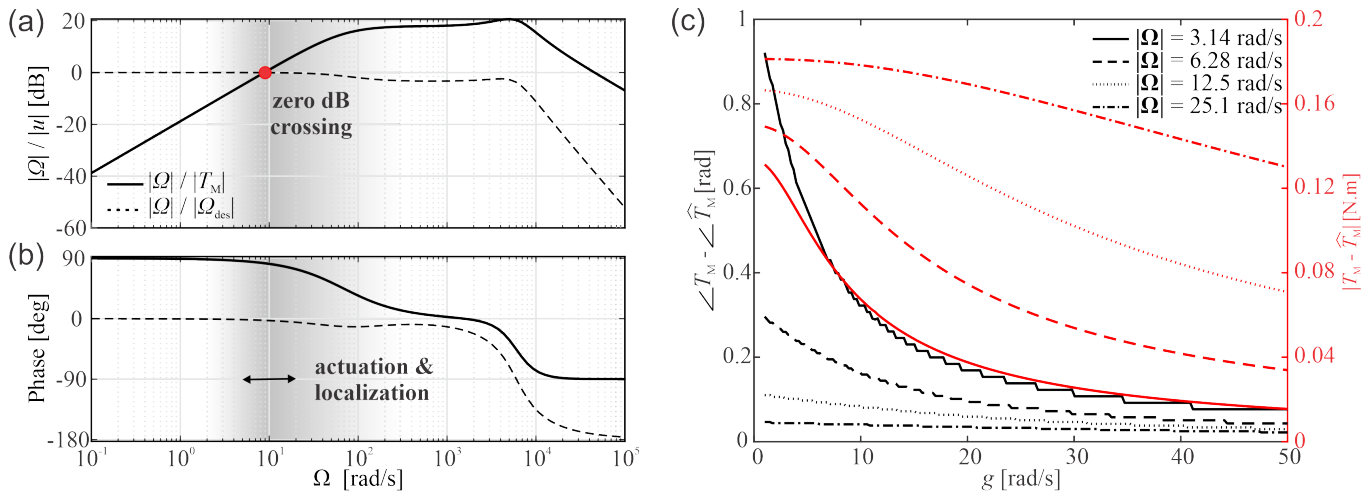

Fig. 4. Amplitude and phase characteristics of the controlled rotating permanent magnet (RPM). a)-b) Zero dB crossing is calculated at approximately 4.5 rad/s. Below and above this frequency magnetic coupling attenuation and amplification are predicted, respectively. The input u represents either the desired angular velocity, Ω_{des}, or the magnetic torque, T_{M}. c) The calculated, T_{M}, and estimated, $\widehat{T}_{\text{M}}$, magnetic torque are determined in terms of the cut-off frequency of the magnetic coupling observer, g. The phase difference, $\angle T_{\text{M}} - \angle \widehat{T}_{\text{M}}$, decreases with g and $\boldsymbol{\Omega}$. The amplitude difference decreases with g and increases with $\boldsymbol{\Omega}$ [47].

of the RPM is controlled using a PI/low-pass filter system, then the corresponding characteristics using the magnitude and phase can be determined based on the nominal parameters of an RPM and a DC motor regardless of the characteristics of the UMR, as shown in Figs. 4(a) and 4(b). The magnitude part of the Bode plot shows magnetic coupling attenuation (solid line) below the zero dB crossing and amplitude independence of the angular velocity (dashed line). Above the zero dB crossing, this independence remains for the angular velocity while magnetic torque amplification is observed. Note that the amplitude and phase characteristics (Figs. 4(a) and 4(b)) are entirely dependent on the dynamics of the actuator ($E(s)$ and $G(s)$) and the control system ($C(s)$). As a result, it will be possible to alter the attenuation and amplification characteristics by appropriately choosing the actuator and the control system. This strategic selection enables the UMR to create detectable torque at the RPM within a designated localization gap. Hence, it is clear that the RPM-UMR gap is not the sole factor in determining the UMR's position. Consider, for example, the UMR and RPM parameters in Table II. In this case, a 12-mm diameter UMR with magnetic moment of $m = 1.12$ A.m^2 at a distance of 0.2 m further away from an RPM with magnetic moment of $M = 18.89$ A.m^2 would produce a magnetic torque of 0.26 mN.m, which would be amplified or attenuated according to $G(s)/1 + C(s)E(s)G(s) + k_{\text{e}}E(s)G(s)$ for a given actuation frequency.

The amplitude characteristics of the system in Eq. 7, with the designated angular frequency, Ω_{des}, and the magnetic coupling, T_{M}, inputs point to a frequency range favorable for localization. Beyond the zero dB crossing, magnetic coupling amplification occurs, creating an area where we can effectively manage the RPM's angular velocity. Remarkably, the same variables used for control can also serve to estimate the magnetic coupling. To obtain an estimation of the overall external coupling on the RPM, it is necessary to measure both the current and angular velocity of the DC motor. Utilizing

TABLE II

MAGNETIC AND GEOMETRIC PARAMETERS OF THE UNTETHERED MAGNETIC DEVICE (UMR), ROTATING PERMANENT MAGNET (RPM), AND THE NOMINAL PARAMETERS OF THE DC MOTOR. r AND m REPRESENT THE RADIUS OF THE UMR AND ITS MAGNETIC MOMENT. THE RPM IS A CYLINDRICAL MAGNET WITH DIAMETER D, HEIGHT h, AND MAGNETIC MOMENT M.

	Property	Value	Property	Value
UMRs	$2r$ [mm]	12	m [A.m^2]	1.12
	Grade	NdFeB (N42)	Remanence [T]	1.31
	$2r$ [mm]	8	m [A.m^2]	0.27
	Grade	NdFeB (N38)	Remanence [T]	1.24
	$2r$ [mm]	5	m [A.m^2]	0.07
	Grade	NdFeB (N42)	Remanence [T]	1.31
	$2r$ [mm]	3	m [A.m^2]	0.01
	Grade	NdFeB (N42)	Remanence [T]	1.31
RPM	$D \times H$ [mm]	35×25	M [A.m^2]	18.89
	Grade	NdFeB (N52)	Remanence [T]	1.43
Motor	J_1 [kg.m^2]	20×10^{-7}	J_2 [kg.m^2]$\times 10^{-5}$	2.03
	B [N.m/rad/s]	3.54×10^{-6}	K_{t} [N.m/A]	0.02
	τ_{e} [s]$\times 10^{-3}$	0.16	τ_{m} [s]$\times 10^{-3}$	6.86
	k_{p} [A.s/rad]	0.041	k_{i} [A/rad]	4.20

Equation (5), we can then estimate T_{M}. The motor's drawn current, a variable available as input, is indicative of the control applied to the RPM's angular velocity. In cases where the angular velocity is quantified to achieve the targeted rotational speed, the wireless actuation of the UMR offers the opportunity to determine the magnetic coupling.

III. MAGNETIC COUPLING ESTIMATION FOR THE UMR

In this section, we introduce a comprehensive model that characterizes the motion of the RPM, which is under robotic control to facilitate UMR actuation and enable the estimation of its magnetic coupling. Experimental results demonstrating this coupling are in Appendix B.

A. Actuation using Permanent Magnet Robotic System

A UMR with a dipole moment can be actuated by the torque $\mathbf{T}_{\text{m}}(\mathbf{p}, \mathbb{M}, \mathbb{m})$ and force $\mathbf{f}_{\text{m}}(\mathbf{p}, \mathbb{M}, \mathbb{m})$ produced by an RPM.

The magnetic force and torque are determined by the actuating magnetic field $\mathbf{B}(\mathbf{p}, \mathbb{M})$. When the RPM is attached to the end-effector of a serial manipulator, the displacement of the RPM can be controlled to exert a desired force and torque on the UMR. Note that a permanent-magnet robotic system is typically a 6-degrees-of-freedom (DOF) serial manipulator to control the displacement of the RPM. The magnetic field at a point $\mathbf{p}$ can be controlled through the joints of the manipulator. The configuration to pose kinematics of the robotic manipulator can be written as

$$\{\mathbf{p}_{\text{act}}, \mathbf{R}\} = \mathcal{F}(\boldsymbol{q}) \ , \ \begin{pmatrix} \dot{\mathbf{p}}_{\text{act}} \\ \boldsymbol{\omega}_{\text{a}} \end{pmatrix} = \mathbf{J}_{\text{m}}(\boldsymbol{q})\dot{\boldsymbol{q}}, \tag{8}$$

where $\mathcal{F} : \mathbb{R}^n \rightarrow \{\mathbb{R}^3, SO(3)\}$ is the forward kinematic mapping, $\mathbf{J}_{\text{m}} \in \mathbb{R}^{n\times n}$ is the geometric Jacobian, and $\boldsymbol{q} \in \mathbb{R}^n$ are the joint variables. The composed linear and angular velocities of the RPM acting as an end-effector in the task space can be related to the joint velocities by the serial manipulator's Jacobian. Mahoney and Abbott have shown that the velocity level kinematics can also be modified to include the contribution of the magnetic moment of the actuator magnet using $\dot{\mathbb{M}} = \boldsymbol{\omega}_{\text{a}} \times \mathbb{M}$, and we obtain [37]

$$\begin{pmatrix} \dot{\mathbf{p}}_{\text{act}} \\ \dot{\mathbb{M}} \end{pmatrix} = \begin{pmatrix} \mathbb{I} & 0 \\ 0 & \text{SK}(\mathbb{M})^{\text{T}} \end{pmatrix} \mathbf{J}_{\text{m}}(\boldsymbol{q})\dot{\boldsymbol{q}} = \mathbf{J}_{\text{A}}(\boldsymbol{q})\dot{\boldsymbol{q}}, \tag{9}$$

where $\text{SK}(\cdot) : \mathbb{R}^3 \rightarrow SO(3)$ is the skew-symmetric operator of the cross product and $\mathbf{J}_{\text{A}} \in \mathbb{R}^{n\times n}$ is the actuator permanent magnet Jacobian. Equation (9) denotes the imparted rate of change in the RPM's net position and heading of the RPM's dipole moment due to the manipulator's joint velocities. The expressions for torque, $\mathbf{T}_{\text{m}}$, and force, $\mathbf{f}_{\text{m}}$, can be linearized as follows:

$$\begin{pmatrix} \dot{\mathbf{f}}_{\text{m}} \\ \dot{\mathbf{T}}_{\text{m}} \end{pmatrix} = \begin{pmatrix} \frac{\partial \mathbf{f}_{\text{m}}}{\partial \mathbf{p}} & \frac{\partial \mathbf{f}_{\text{m}}}{\partial \mathbb{M}} & \frac{\partial \mathbf{f}_{\text{m}}}{\partial \hat{\mathbf{m}}} \\ \frac{\partial \mathbf{T}_{\text{m}}}{\partial \mathbf{p}} & \frac{\partial \mathbf{T}_{\text{m}}}{\partial \mathbb{M}} & \frac{\partial \mathbf{T}_{\text{m}}}{\partial \hat{\mathbf{m}}} \end{pmatrix} \begin{pmatrix} \dot{\mathbf{p}} \\ \dot{\mathbb{M}} \\ \dot{\mathbb{m}} \end{pmatrix}. \tag{10}$$

If we use Equations (8) and (10) to create a magnetic coupling that can be estimated using Equation (5), the localization problem becomes one of estimating T_{M} which would depend on the location of the UMR and the RPM, and their magnetic characteristics.

B. Magnetic Coupling Estimation and Trades

Let us now consider the rotational dynamics of the RPM (5) and the magnetic coupling (4). This single-input single-output system is magnetically coupled as a result of the interactions between the RPM and the UMR. The following observer can exponentially track the disturbance through angular velocity and current measurements [38], [39], [40]:

$$\widehat{T}_{\text{M}} = \frac{g}{s+g}\left(Jg\Omega + I_{\text{a}}K_{\text{t}}\right) - Jg\Omega, \tag{11}$$

where $g \in \mathbb{R}^+$ is the cut-off frequency of the observer and J is the inertia of the motor and the RPM. Equipped with the nominal parameters (Table II) of the DC-motor and the current and angular velocity, the magnetic coupling can be determined. Note that the phase delay and error between the magnetic torque, T_{M}, and its estimate, $\widehat{T}_{\text{M}}$, can be made arbitrarily small by increasing the cut-off frequency of the observer (11), as shown in Fig. 4(c). In general, choosing $g > 0$ guarantees that $|T_{\text{M}}(t) - \widehat{T}_{\text{M}}|$ tends to zero as t tends to infinity and the convergence rate can be adjusted by choice of g. Fig. 4(c) also provides the convergence rates for various actuation frequencies in the $0.5 \leq |\Omega| \leq 4$ Hz range. Although there exists a frequency range above the zero dB crossing (Fig. 4(a)) that yields a desirable amplification of the magnetic torque, the estimation error increases with Ω. Therefore, increasing the actuation frequency of the UMR will introduce undesirable attenuation in the magnetic coupling, causing the estimation error to increase regardless of the cut-off frequency of the observer. This trade-off between actuation frequency and magnetic coupling estimation error imposes a limitation on the speed of the UMR during simultaneous localization and actuation.

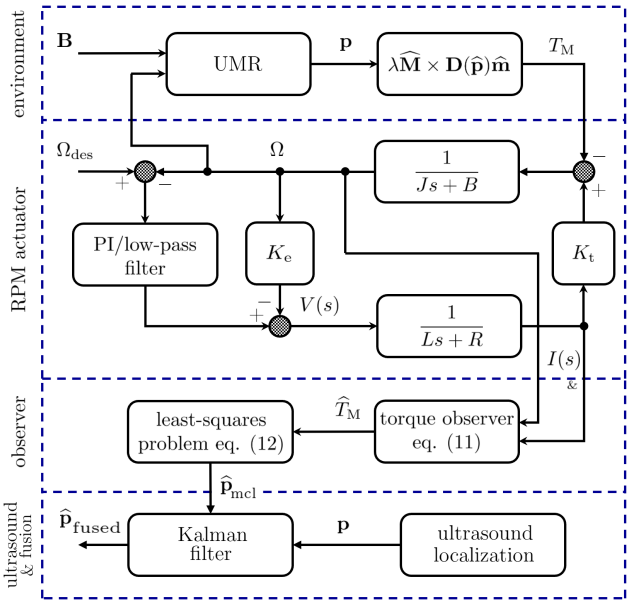

Fig. 5. When controlling the RPM to a desired angular velocity, Ω_{des}, the rotating magnetic field exerts a magnetic torque on the UMR, which causes the UMR to move. The relative motion between the UMR and the RPM affects the angular velocity, Ω, and induces a back-emf, $K_e\Omega$, which counteracts the applied voltage. The change in the applied current and velocity are used to estimate the magnetic torque, $\widehat{T}_{\text{M}}$, and the position of the UMR, $\widehat{\mathbf{p}}_{\text{mcl}}$. This approximation is passed to the Kalman filter, along with $\mathbf{p}$ from ultrasound localization. The Kalman filter produces the fused position of the UMR, $\widehat{\mathbf{p}}_{\text{fused}}$.

IV. Actuation and Localization of UMRs

If the UMR is actuated to rotate in sync with the RPM, then the orientation of the magnetization vector $\mathbf{m}$ can be determined based on the orientation of $\mathbf{M}$. In this scenario, $\mathbf{m}$ lags behind $\mathbf{M}$ when the frequency is below the step-out frequency. It is important to highlight that the orientation of the magnetization vector $\mathbf{M}$ can be reconstructed using the manipulator's joint space variables $\boldsymbol{q}$, as outlined by the kinematic relation (8). Consequently, the magnitude and orientation of the RPM are accurately known, facilitating the estimation of the magnetic coupling through measurements of the current and angular velocity.

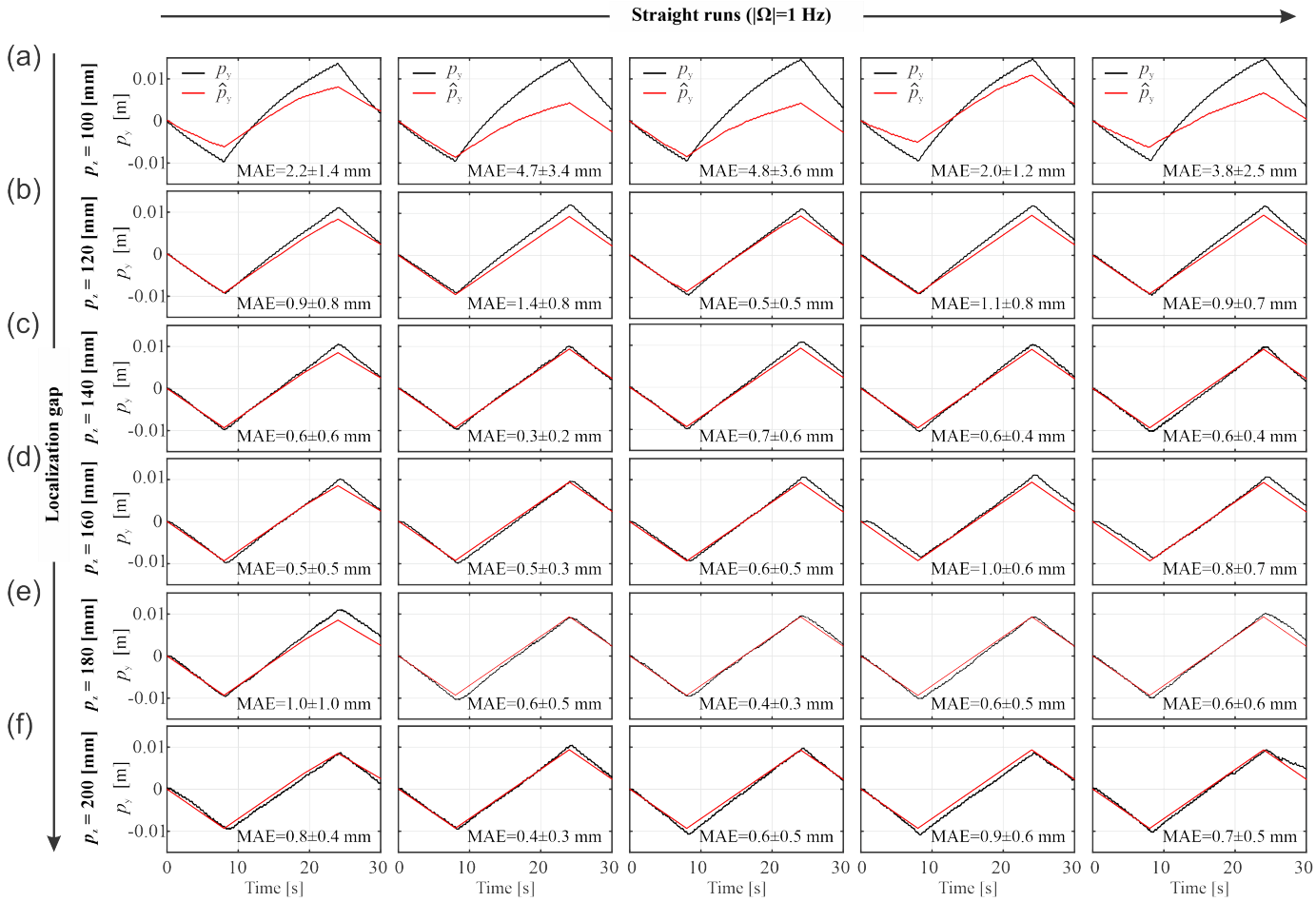

Fig. 6. Prediction of the localization performance by the model suggests actuation and localization at the zero db crossing ($\approx$ 1 Hz). The UMR is allowed to roll back and forth along the $\mathbf{y}$-axis of the tube. The position of the UMR is measured to validate the numerical results of equations (1)-(10). a) For $p_z = 100$ mm, maximum MAE is 4.8 ± 3.6 mm. b) For $p_z = 120$ mm, maximum MAE is 1.4 ± 0.8 mm. c) For $p_z = 140$ mm, maximum MAE is 0.7 ± 0.6 mm. d) For $p_z = 160$ mm, maximum MAE is 1.0 ± 0.6 mm. e) For $p_z = 180$ mm, maximum MAE is 1.0 ± 1.0 mm. f) For $p_z = 200$ mm, maximum MAE is 0.9 ± 0.6 mm.

A. Localization of the UMR

The localization problem of the UMR is solved by minimizing the following objective function:

$$\epsilon = \min_{\mathbf{p}} \left\{ \left\| \widehat{\mathbf{T}}_{\mathbf{m}} - \frac{\mu_0 \|\mathbf{M}\| \|\mathbf{m}\|}{4\pi \|\mathbf{p}\|^3} \mathbb{M} \times D(\mathrm{p}) \mathrm{m} \right\|^2 \right\}, \quad (12)$$

with respect to $\mathbf{p}$. The first term in Equation (12) is computed employing the magnetic coupling observer (11), while the second term is formulated using the robotic manipulator's joint variables during magnetic actuation, based on Equation (8). The distinct components of this localization technique can be visually represented through a block diagram, as depicted in Fig. 5.

Upon applying a rotating magnetic field, $\mathbf{B}$, to the UMR, it will undergo motion relative to the RPM, and its position can be described by $\mathbf{p}$. However, unless the smallest detectable torque, T_{M}, is not equal to zero, there will not be a generated back-emf, nor an elevation in the drawn current to offset the applied voltage through coupling. There is another important role for the dynamics of the RPM actuator in the localization rate. Unless the mechanical (i.e., in $1/(Js + B)$) and magnetic (i.e., in $1/(Ls + R)$) inertia of the RPM actuator are zero, the angular velocity, Ω, and the current, I, cannot rise immediately, respectively (Figs. 12(b) and 12(c)). In contrast to the preferable rapid increase in current and velocity, the RPM actuator necessitates operation within a closed-loop system. In this scenario, enhancing the overall gain of the feedback system becomes advantageous to enhance disturbance rejection and minimize the impact of measurement noise sensitivity [41]. This constitutes a second trade-off between closed-loop actuation and localization. Assuming that the RPM actuator is designed with impeccable mechanical and magnetic inertia, enabling the UMR's magnetic torque to prompt an instantaneous rise in current and velocity, the performance could still degrade during actuation.

B. Simultaneous localization and actuation

A practical way to test the localization is to move the UMR by rolling in the $\boldsymbol{y}$-axis inside the lumen. In this case, the ability of the observer to estimate the position of the UMR is tested for a localization gap greater than 100 mm (10 body lengths), as shown in Fig. 6. Fig. 4(c) shows that in the limit

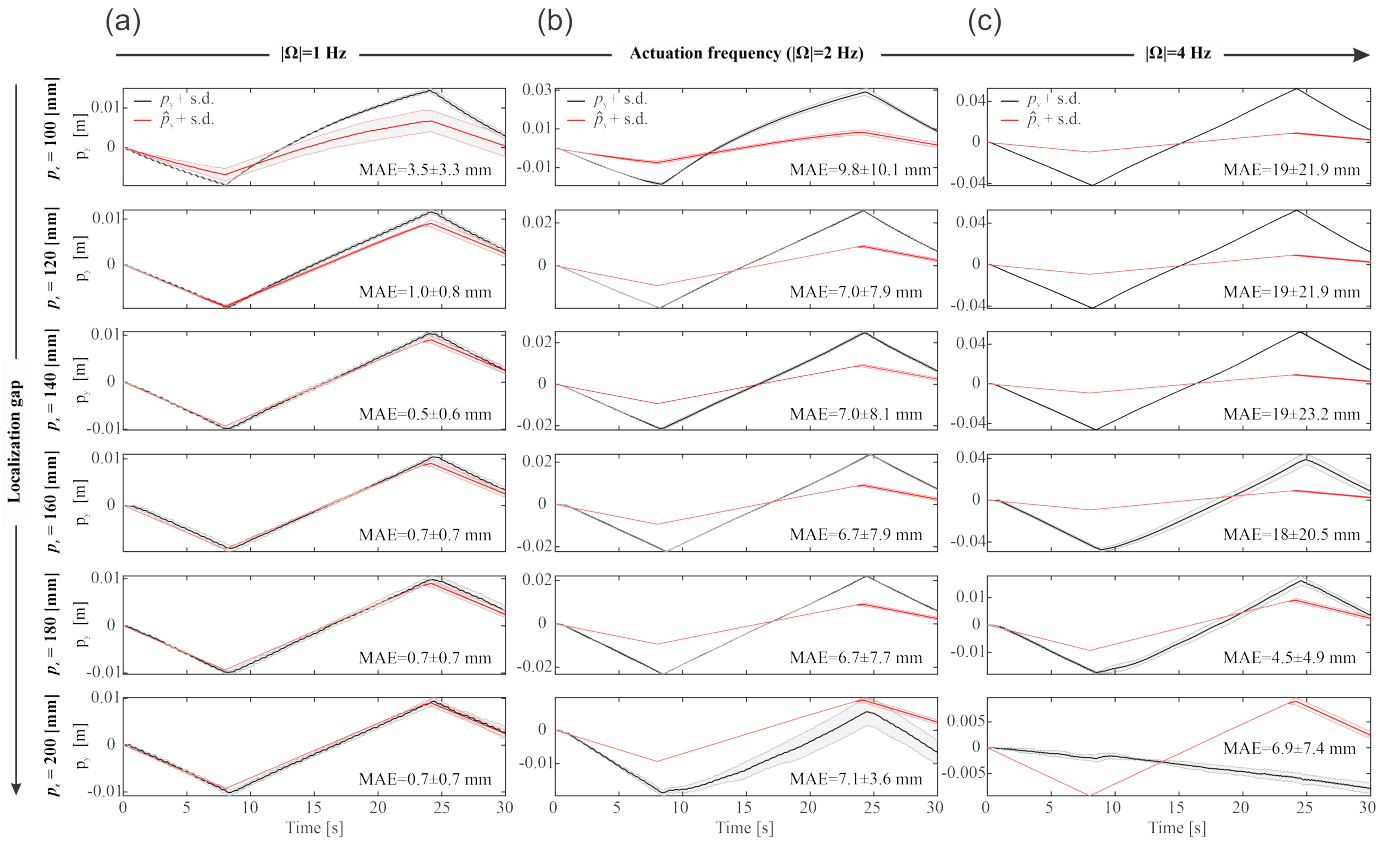

Fig. 7. The magnetic torque estimation error at low-actuation frequency can be made small (see Fig. 4(c)), resulting in minimal localization error for a given observer gain. The UMR is allowed to roll back and forth along the $\mathbf{y}$-axis of the tube. The position of the UMR is measured to validate the numerical results of equations (1)-(10). a) $|\mathbf{\Omega}| = 1$ Hz and $100 \leq p_z \leq 200$ mm, maximum MAE is 3.5 ± 3.3 mm b) $|\mathbf{\Omega}| = 2$ Hz and $100 \leq p_z \leq 200$ mm, maximum MAE is 9.8 ± 10.1 mm c) $|\mathbf{\Omega}| = 4$ Hz and $100 \leq p_z \leq 200$ mm, maximum MAE is 19.23 ± 3.3 mm. The localization method fails to capture the qualitative behavior of the UMR for $p_z = 200$ mm and $|\mathbf{\Omega}| = 4$ Hz.

of very small actuation frequency and large observer gain, it is reasonable to obtain the smallest magnetic coupling estimation error. Therefore, we actuate the UMR at 1 Hz and increase the localization gap gradually. Multiple horizontal runs ($n = 5$) for a localization gap of $p_z = 100$ mm (Fig. 6(a)) shows maximum MAE of 4.8 ± 3.6 mm. Increasing the gap to $p_z = 120$ mm (Fig. 6(b)) shows that the maximum MAE decreases to 1.4 ± 0.8 mm for the same actuation frequency, $\mathbf{\Omega}$, and observer gain, g. Similarly, the maximum MAE of five trials for a localization gap of $p_z = 140$ mm decreases to 0.7 ± 0.6 mm, as shown in Fig. 6(c). Note that for a relatively small localization gap, the field-gradient pulling between the RPM and the UMR generates additional friction on the rotor of the actuator. As the gap increases, the field-gradient pulling becomes negligible and the additional friction decreases, resulting in a smaller magnetic coupling estimation error. This behavior is shown for greater localization gaps of 160 mm, 180 mm, and 200 mm, as shown in Figs. 6(d)-6(f), respectively.

Now we turn to the role of the actuation frequency on the localization error, as shown in Fig. 7. Similarly, we allow the UMR to have multiple horizontal runs along the $\boldsymbol{y}$-axis for a range of localization gap, $100 \leq p_y \leq 200$ mm. It is expected that the smaller magnetic coupling estimation error is possible at low actuation frequency (Fig. 4(c)), resulting in a smaller localization error. This result is shown in Fig. 7(a) for actuation frequency $|\mathbf{\Omega}| = 1$ Hz whose maximum MAE is measured as 3.5 ± 3.3 mm for localization gap of 100 mm. Increasing the actuation frequency to $|\mathbf{\Omega}| = 2$ Hz (Fig. 7(b)) results in greater localization error with a maximum MAE of 9.8 ± 10.1 mm for a localization gap of 100 mm. Increasing the actuation frequency further to $|\mathbf{\Omega}| = 4$ Hz results in an increased localization error with a maximum MAE of 19 ± 21.9 mm, as shown in Fig. 7(c). Therefore, when the minimum localization gap is set to 10 body lengths the smallest MAE occurs at the lowest actuation frequency. This localization result suggests that our localization experiment is in agreement with the theoretical predictions in Fig. 4(c). It suggests that the estimation error between the actual and estimated magnetic torque increases with the actuation frequency for a given observer gain. Therefore, minimum error in the estimated magnetic coupling occurs when the UMR is actuated at a low actuation frequency of 1 Hz, resulting in a slight amplification of the magnetic coupling torque (Fig. 4(a)) since the zero dB crossing is calculated at 0.7 Hz.

C. Localization of millimeter-sized UMRs

Given that minimizing the size of the UMR is vital to navigating through confined spaces, we proceed to assess the effectiveness of our MCL approach using UMRs falling within the $3 \leq 2r \leq 12$ mm range, as shown in Fig. 8. Here, we

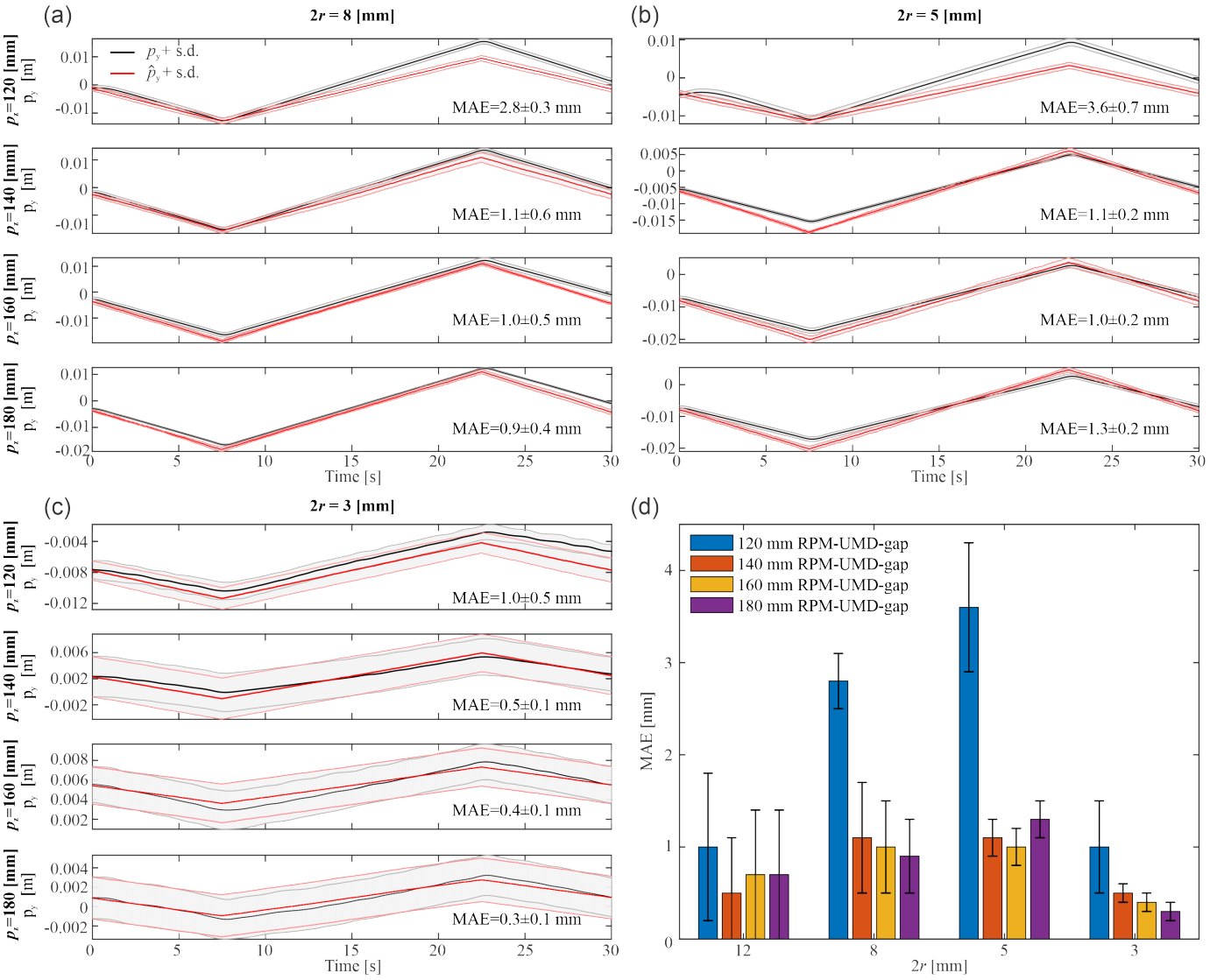

Fig. 8. MCL is implemented using an 8-mm, a 5-mm, and a 3-mm UMR, at actuation frequency of 1 Hz. Below and above the RPM-UMR gap of 120 mm and 180 mm, rolling is not possible because of the field-gradient pulling and decreased magnetic torque, respectively. a) At the RPM-UMR gap of 180 mm, the measured MAE of the 8-mm UMR is 0.9 ± 0.4 mm. b) At the RPM-UMR gap of 180 mm, the measured MAE of the 5-mm UMR is 1.3 ± 0.2 mm. c) At the RPM-UMR gap of 180 mm, the MAE of a 3-mm UMR is 0.3 ± 0.1 mm. d) The MAE is measured for UMRs and localization gap in the range of $3 \leq 2r < 12$ mm and $120 \leq p_z \leq 180$ mm, respectively.

enable UMRs with diameters of 8 mm, 5 mm, and 3 mm to roll along the $\boldsymbol{y}$-axis within the lumen. This motion is guided by a rotating magnetic field with an actuation frequency of 1 Hz, as in the preceding trials. In these cases, the RPM-UMR gap is confined within the range of 120 mm to 180 mm. Within this defined localization gap, we observe a reasonable rolling response across all four UMRs. However, as the UMR diameter decreases, its response to both the field-gradient pulling and the influence of gravity is noticeably affected.

Fig. 8(a) shows the behavior of an 8-mm UMR along the $\boldsymbol{y}$-axis in relation to the estimated position component. Except for the 120 mm RPM-UMR gap, the MAE demonstrates a relatively consistent pattern as this gap gradually extends up to 180 mm. Similarly to the case of the 8-mm UMR, Fig. 8(b) reveals that the highest MAE for a 5-mm UMR is computed for the smallest RPM-UMR gap of 120 mm. As this gap gradually increases, the MAE experiences a minor reduction within the range of 140 mm to 180 mm. Specifically, at an RPM-UMR gap of 140 mm, the average MAE is calculated to be 1.1 ± 0.2 mm, and this value increases to 1.3 ± 0.2 mm as the gap reaches 180 mm.

Using a 3-mm UMR within the same gap as previously mentioned, achieving an identical range of motion along the $\boldsymbol{y}$-axis was not feasible. This disparity can be attributed to the reduced influence of magnetic torque on its magnetic moment, which is proportional to its diameter. Furthermore, the weight of the UMR is exponentially reduced as its mass is proportional to r^3, resulting in lower traction with the lumen wall. Fig. 8(c) shows the reciprocal motion of the 3-mm UMR. Consistently with prior cases, the highest MAE is observed at an RPM-UMR gap of 120 mm. At this gap, the calculated MAE is 1.0 ± 0.5 mm. However, as the gap gradually increases

from 140 mm to 180 mm, the MAE decreases from 0.5 ± 0.1 mm to 0.3 ± 0.1 mm.

Fig. 8(d) shows the effect of downscaling and localization gap on the average MAE. Throughout these trials, all UMRs are controlled to roll while being subjected to a rotating magnetic field of 1 Hz. Additionally, a consistent observer gain is employed across these experiments. It is clear from our observations that the localization accuracy of our MCL approach is influenced by the UMR's response to the field-gradient pulling. Across all UMR sizes, the highest MAE is observed at a gap of 120 mm. Nevertheless, regardless of the UMR's dimensions, as the gap surpasses 120 mm and the impact of the field-gradient pulling diminishes, a significant reduction in MAE is consistently observed for all UMRs.

Fig. 8(d) shows the lowest MAE for the 3-mm UMR, but it cannot be definitively stated that there is a singular best size overall. For example, when considering the 12-mm UMR, it is apparent that MCL provides a much more consistent performance across varying gaps. This increased consistency in performance might be a more desirable characteristic in some situations.

V. Hybrid Approach through Fusion of Magnetic Coupling Localization and Ultrasound Localization

A. Ultrasound images

Ultrasound waves can undergo absorption or attenuation as they propagate through a medium. In this case, the magnetic coupling between the UMR and the RPM-actuator offers supplementary insights, provided that this magnetic coupling can be detected through the actuator's sensor data. While MCL relies on the current and angular velocity of the RPM actuator to estimate the UMR's position, ultrasound images provide a more comprehensive view of the UMR and its surroundings, as depicted in Fig. 9(b). In this trial, the UMR is allowed to move along the $\boldsymbol{y}$-axis under the influence of a rotating magnetic field about the $\boldsymbol{x}$-axis, in the frame of reference depicted in Fig. 2. It is anticipated that localization interruptions may occur due to wave reflectors. These interruptions are simulated in Fig. 2 as a pattern of data loss. This pattern is artificially induced on the measured position of the UMR from the gathered ultrasound images. In practice, this pattern could exhibit a time-periodic nature, and the delay can be correlated with image processing to track the UMR and reconstruct the environment. The data loss pattern may also depend on the spatial and temporal properties of the wave reflectors within the environment. In contrast to ultrasound images, MCL provides a faster and permanent signal as long as the UMR is magnetically coupled with its RPM-actuator. Therefore, we use a Kalman Filter configuration to predict the response of the UMR in situations where random data loss is encountered.

B. Data Fusion

Expanding on the system dynamics in Appendix C, at low Reynolds numbers, the behavior of a UMR with a radius of r

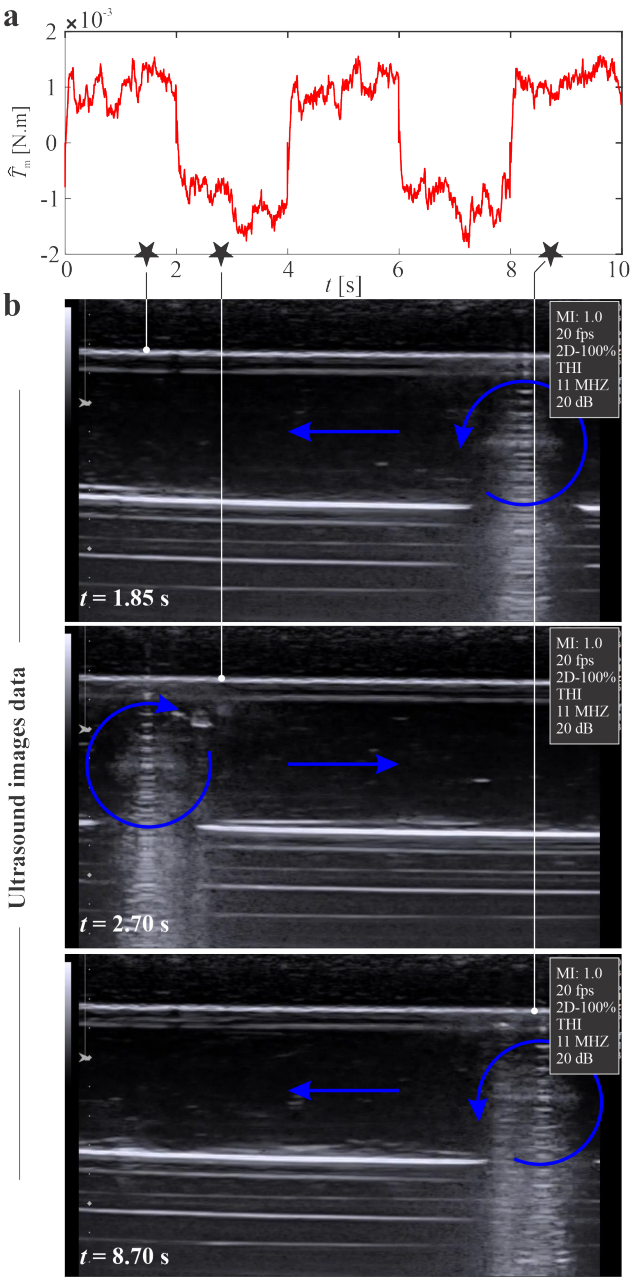

Fig. 9. The UMR is allowed to roll inside a fluid-filled lumen and inputs are measured from two sensors. (a) The magnetic coupling between the UMR and the RPM actuator is estimated using MCL. (b) Ultrasound images are simultaneously collected. The white and red arrows indicate the direction of motion and rotation of the UMR, respectively.

is defined by the equilibrium between magnetic forces, drag forces, contact forces, and torques, such that

$$\begin{pmatrix} \dot{\mathbf{p}} \\ \boldsymbol{\omega} \end{pmatrix} = \frac{-1}{\pi\eta} \begin{pmatrix} 6f_{\mathrm{t}}r & 6f_{\mathrm{t}}r^2 \\ 8T_{\mathrm{t}}r^2 & 8T_{\mathrm{r}}r^3 \end{pmatrix}^{-1} \left\{ \begin{pmatrix} \mathbf{f}_{\mathrm{m}} \\ \mathbf{T}_{\mathrm{m}} \end{pmatrix} + \begin{pmatrix} \mathbf{f}_{\mathrm{c}} \\ \mathbf{T}_{\mathrm{c}} \end{pmatrix} \right\}, \quad (13)$$

where $\mathbf{f}_{\mathrm{m}}$ and $\mathbf{f}_{\mathrm{c}}$ represent the magnetic force and contact force, while $\mathbf{T}_{\mathrm{m}}$ and $\mathbf{T}_{\mathrm{c}}$ denote their respective torques. Further, f_{t} and f_{r} represent normalized scalar near-wall fluid forces for translational and rotational motion, respectively, while T_{t} and T_{r} are their respective normalized scalar torques. Below the step-out frequency of the UMR, it rotates in sync

with a rotating magnetic field of the RPM. Using Eq. 13, ignoring rotational dynamics we get

$$\dot{\mathbf{p}} = \underbrace{\frac{1}{2\pi\mu r(T_\mathrm{r}-T_\mathrm{t})}}_{K}\left(\underbrace{\frac{T_\mathrm{r}}{3f_\mathrm{t}}\left(\mathbf{f}_\mathrm{m}+f_\mathrm{c}\right)}_{\mathbf{L}}-\underbrace{\frac{1}{4r}\left(\mathbf{T}_\mathrm{m}+T_\mathrm{c}\right)}_{\mathbf{R}}\right), \tag{14}$$

where we define K, $\mathbf{L}$, and $\mathbf{R}$ for compactness. The resulting state space, which represents the internal model of the Kalman Filter becomes

$$\underbrace{\begin{bmatrix}\dot{\mathbf{p}}\\ \ddot{\mathbf{p}}\end{bmatrix}}_{\dot{\mathbf{x}}} = \underbrace{\begin{bmatrix}0 & 1\\ 0 & 0\end{bmatrix}}_{\mathbf{A}}\underbrace{\begin{bmatrix}\mathbf{p}\\ K(L-R)\end{bmatrix}}_{\mathbf{x}} + \underbrace{\begin{bmatrix}\boldsymbol{w}\\ 0\end{bmatrix}}_{\overline{\boldsymbol{w}}}. \tag{15}$$

The Kalman Filter, with Eq. 15, is employed to estimate the position of the UMR by fusing ultrasound localization and MCL approximations. These measurements are represented as inputs for the Kalman Filter by $\mathbf{y}_\mathrm{us}$ and $\mathbf{y}_\mathrm{mcl}$ respectively. This produces

$$\underbrace{\begin{bmatrix}\mathbf{y}_\mathrm{us}\\ \mathbf{y}_\mathrm{mcl}\end{bmatrix}}_{\mathbf{y}} = \underbrace{\begin{bmatrix}1 & 0\\ 0 & 1\end{bmatrix}}_{\mathbf{C}}\underbrace{\begin{bmatrix}\mathbf{p}\\ \dot{\mathbf{p}}\end{bmatrix}}_{\mathbf{x}} + \underbrace{\begin{bmatrix}\boldsymbol{v}_\mathrm{us}\\ \boldsymbol{v}_\mathrm{mcl}\end{bmatrix}}_{\overline{\boldsymbol{v}}}, \tag{16}$$

where $\overline{\boldsymbol{v}}$ denotes the observation noise vectors $\boldsymbol{v}_\mathrm{us}$ and $\boldsymbol{v}_\mathrm{mcl}$. The disturbance and the observation noises are considered uncorrelated, zero-mean, white Gaussian random noise vectors, each with its respective covariance matrix: $\mathbf{Q} \geq 0$ for disturbances and $\mathbf{R} \geq 0$ for observation noise. The corresponding discrete-time linear system can be written as

$$\mathbf{x}_{k+1} = \begin{bmatrix}1 & \frac{1}{fs}\\ 0 & 1\end{bmatrix}\mathbf{x}_k + \begin{bmatrix}\boldsymbol{w}_k\\ 0\end{bmatrix}, \tag{17}$$

$$\begin{bmatrix}\mathbf{y}_{\mathrm{us},k}\\ \mathbf{y}_{\mathrm{mcl},k}\end{bmatrix} = \begin{bmatrix}1 & 0\\ 0 & 1\end{bmatrix}\mathbf{x}_k + \begin{bmatrix}\boldsymbol{v}_{\mathrm{us},k}\\ \boldsymbol{v}_{\mathrm{mcl},k}\end{bmatrix}. \tag{18}$$

Here, the subscript k signifies the time index. The system and observation matrices have dimensions that match appropriately. Consequently, the Kalman Filter achieves convergence with periodic observation updates, assuming no missing measurements and observability of $(\mathbf{A}, \mathbf{C})$ is observable. In our case, we account for the possibility that $\mathbf{y}_{\mathrm{us},k}$ and $\mathbf{y}_{\mathrm{mcl},k}$, which correspond to US and MCL observations, could be absent during certain time instances. We use i.i.d. Bernoulli variables $\alpha_{i,k}, \quad i = 1, 2$, that take values 1 or 0 to define whether $y_{i,t}$ is missing or received at time t. The case of missing data corresponds to an infinite noise variance for the relevant data source. The prediction step remains unchanged from the standard Kalman Filter, as it is independent of the observation process, and we have

$$\hat{\mathbf{x}}_{k+1|k} = \mathbf{A}\hat{\mathbf{x}}_{k|k}, \tag{19}$$

$$\mathbf{P}_{k+1|k} = \mathbf{A}\mathbf{P}_{k|k}\mathbf{A}^T + \mathbf{Q}. \tag{20}$$

Conversely, the correction step is now influenced by the stochastic values of the variables $\alpha_{\mathrm{us},k}$ and $\alpha_{\mathrm{mcl},k}$. When $\alpha_{\mathrm{us},k} = \alpha_{\mathrm{mcl},k} = 1$, it signifies the normal condition where both $\mathbf{y}_{\mathrm{us},k}$ and $\mathbf{y}_{\mathrm{mcl},k}$ are available. In this case, the correction step is given by

$$\hat{\mathbf{x}}_{k+1|k+1} = \hat{\mathbf{x}}_{k+1|k} + \mathbf{P}_{k+1|k}\mathbf{C}^T\left[\mathbf{C}\mathbf{P}_{k+1|k}\mathbf{C}^T + \mathbf{R}\right]^{-1}\left(\mathbf{y}_{k+1} - \mathbf{C}\hat{\mathbf{x}}_{k+1|k}\right), \tag{21}$$

$$\mathbf{P}_{k+1|k+1} = \mathbf{P}_{k+1|k} - \mathbf{P}_{k+1|k}\mathbf{C}^T\left[\mathbf{C}\mathbf{P}_{k+1|k}\mathbf{C}^T + \mathbf{R}\right]^{-1}\mathbf{C}\mathbf{P}_{k+1|k}. \tag{22}$$

When $\alpha_{\mathrm{us},k} = \alpha_{\mathrm{mcl},k} = 0$, it signifies a lack of available data from both sensors, and the correction step involves executing the open loop procedure described by

$$\hat{\mathbf{x}}_{k+1|k+1} = \hat{\mathbf{x}}_{k+1|k}, \tag{23}$$

$$\mathbf{P}_{k+1|k+1} = \mathbf{P}_{k+1|k}. \tag{24}$$

Furthermore, $\alpha_{\mathrm{us},k} = 1$ and $\alpha_{\mathrm{mcl},k} = 0$ means that $\mathbf{y}_{\mathrm{us},k}$ is received while $\mathbf{y}_{\mathrm{mcl},k}$ is missing at that time instant corresponding the following noise covariance matrix with an infinite noise variance $\sigma_i^2 \to \infty$ for $\mathbf{y}_{\mathrm{mcl},k}$:

$$\bar{\mathbf{R}} = \begin{bmatrix}\mathbf{R}_{11} & \mathbf{R}_{12}\\ \mathbf{R}_{21} & \sigma^2\mathbf{I}\end{bmatrix}. \tag{25}$$

Therefore the correction step is performed by the noise covariance $\bar{\mathbf{R}}$:

$$\hat{\mathbf{x}}_{k+1|k+1} = \hat{\mathbf{x}}_{k+1|k} + \mathbf{P}_{k+1|k}\mathbf{C}^T\left[\mathbf{C}\mathbf{P}_{k+1|k}\mathbf{C}^T + \bar{\mathbf{R}}\right]^{-1}\left(\mathbf{y}_{k+1} - \mathbf{C}\hat{x}_{k+1|k}\right), \tag{26}$$

$$\mathbf{P}_{k+1|k+1} = \mathbf{P}_{k+1|k} - \mathbf{P}_{k+1|k}\mathbf{C}^T\left[\mathbf{C}\mathbf{P}_{k+1|k}\mathbf{C}^T + \bar{\mathbf{R}}\right]^{-1}\mathbf{C}\mathbf{P}_{k+1|k}. \tag{27}$$

In situations where $\alpha_{\mathrm{us},k} = 0$ and $\alpha_{\mathrm{mcl},k} = 1$, the Kalman Filter exclusively takes $\mathbf{y}_{\mathrm{mcl},k}$ into account as the received data and adjusts accordingly. Employing the simplified notation $\mathbf{P}_k = \mathbf{P}_{k|k-1}$, we can consolidate the preceding correction steps to update the error covariance matrix, thus presenting a generalized Kalman Filtering update procedure that accommodates instances of missing data, as given by [45]:

$$\begin{aligned}\mathbf{P}_{k+1} =& \mathbf{A}\mathbf{P}_k\mathbf{A}^T + \mathbf{Q}\\ &-\alpha_{\mathrm{us},k}\alpha_{\mathrm{mcl},k}\mathbf{A}\mathbf{P}_k\mathbf{C}^T\left[\mathbf{C}\mathbf{P}_k\mathbf{C}^T + \mathbf{R}\right]^{-1}\mathbf{C}\mathbf{P}_t\mathbf{A}^T\\ &-\alpha_{\mathrm{us},k}\left(1-\alpha_{\mathrm{mcl},k}\right)\mathbf{A}\mathbf{P}_k\mathbf{C}_1^T\left[\mathbf{C}_1\mathbf{P}_k\mathbf{C}_1^T + \mathbf{R}_{11}\right]^{-1}\mathbf{C}_1\mathbf{P}_k\mathbf{A}^T\\ &-(1-\alpha_{\mathrm{us},k})\alpha_{\mathrm{mcl},k}\mathbf{A}\mathbf{P}_k\mathbf{C}_2^T\left[\mathbf{C}_2\mathbf{P}_k\mathbf{C}_2^T + \mathbf{R}_{22}\right]^{-1}\mathbf{C}_2\mathbf{P}_k\mathbf{A}^T,\end{aligned} \tag{28}$$

where $\mathbf{C_1}$ and $\mathbf{C_2}$ are the top and bottom rows of $\mathbf{C}$, respectively. The state prediction update within the framework of Kalman Filtering can be extended using a similar approach. Because of the involvement of random variables, the Kalman Filter iteration becomes stochastic in nature.

VI. Performance Evaluation of Data Fusion

A. Experimental Setup

To experimentally verify our sensor fusion technique, we integrate a permanent-magnet wireless manipulation system, an ultrasound imaging system, and a blood vessel phantom, as shown in Fig. 1.

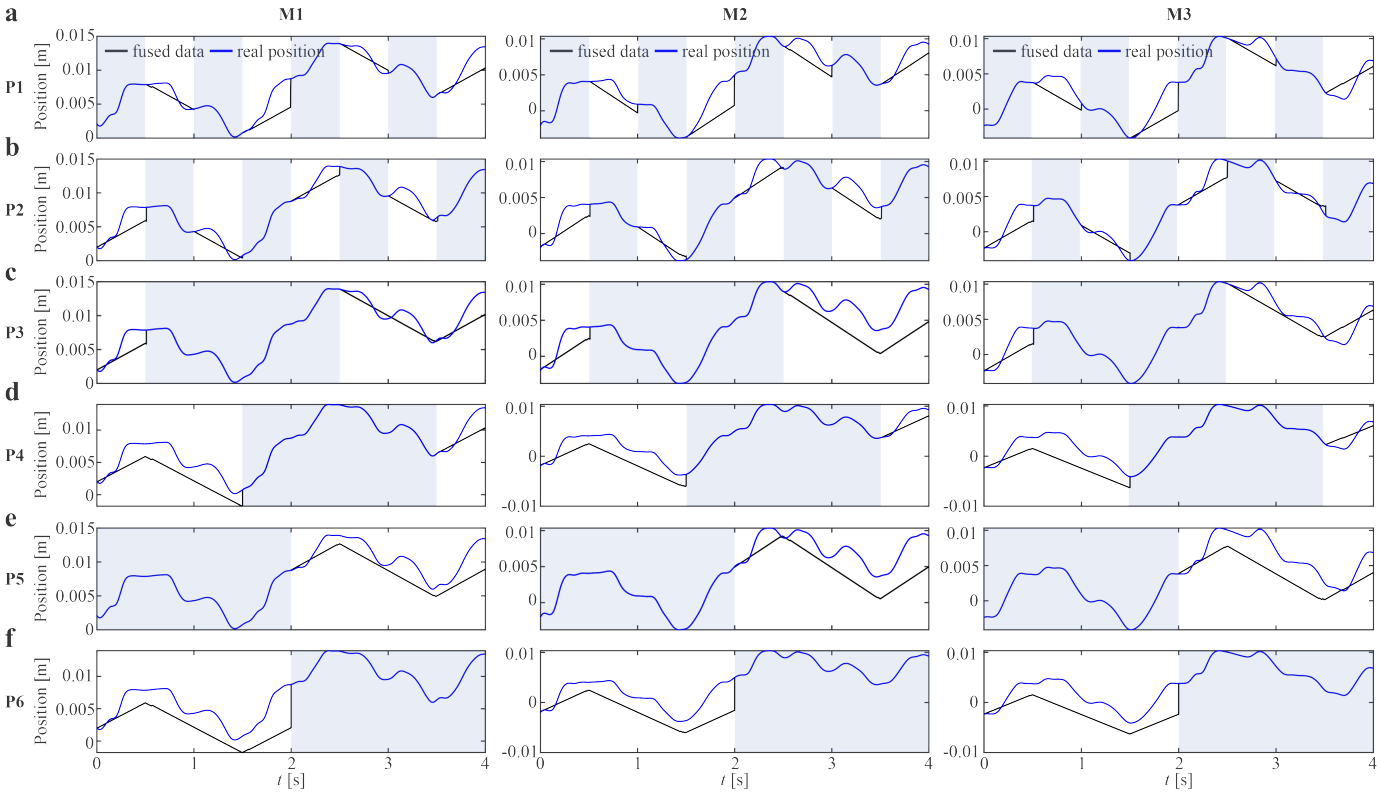

Fig. 10. The fused position data is compared to the real position of the UMR, indicated by a black and blue line respectively. The blue-shaded regions indicate areas where both US and MCL are available. The non-shaded regions are where our method becomes useful as no US localization is available. The fused signal fully relies on MCL and can approximate the velocity as well as directional changes. The columns (M1-M3) are the three individual measurements and the rows (P1-P6) represent the four ultrasound interruption patterns. The top two rows (P1&P2) have shorter (0.5 s) periodic interruptions. These show the fused signal performing accurately in estimating the location of the UMR with minimal error. The bottom four (P3-P6), with longer (2 seconds) interruptions, show a slightly larger absolute error, but they're still able to estimate the directional changes and velocity of the UMR to a degree still useful in determining the location. The error is larger as it can build up for a longer time before being reset by US localization to the real position.

1) Blood Vessel Phantom: The UMR is actuated and localized inside a phantom (275 mm$\times$30 mm$\times$15 mm block), consisting of a muscle, fat, and skin layer (Fig. 2). The muscle layer surrounds a tube with a 12 mm internal diameter that is 350 mm long, which contains porcine blood, and a UMR with a diameter of 8 mm, the properties of which can be seen in Table II. The muscle layer is made of silicone (EcoflexTM 00-30) and prepared with Silc PigTM blood pigment according to the manufacturer's instructions using a WASSERMAN Wamix Touch vacuum mixer. The fat layer is assembled on top of the muscle layer. Silicone (EcoflexTM 00-30) for the fat layer is prepared with Silc PigTM Yellow pigment. Finally, the skin layer is assembled on top of the fat layer. Silicone (EcoflexTM 00-30) for the skin layer is prepared with Silc PigTM flesh tone pigment.

2) Wireless Manipulation System: The control of the RPM, and by extension, the actuation of the UMR was achieved with the KUKA serial manipulator, brushless DC motor, and RPM in Section VIII. The properties of which are in Table II.

3) Ultrasound Localization System: The medical imaging is constructed using a medical-grade ultrasound machine (Siemens Acuson S2000, Berlin, Germany) with a 3D/4D linear array transducer (Siemens 14L5 Linear Array Transducer, Berlin, Germany.) The transducer has a field of view of 38mm and a frequency range of 5.0 - 14.0 MHz. The UMR is located automatically using a contrast-based localization algorithm.

B. Performance Metrics

The performance of the Kalman Filter was evaluated over the segments where the US-localization is interrupted and the Kalman Filter fully relies on MCL and its internal model for its reconstruction of the UMR's position. To investigate the performance fairly, three measurements are simulated to have US localization interruptions according to six predefined patterns, resulting in 18 trials. The two localization modes are processed by the Kalman Filter as described in Section V-B. The 18 resulting trials can be seen in Fig. 10. The shaded region is where both MCL and US signals are present. In these regions, the fused signal accurately follows the real position of UMR. The non-shaded regions are where the Kalman Filter only receives MCL measurements and the US localization is interrupted. This is where our data fusion method becomes useful. in P1 and P2, which are short patterns of periodic interruptions, show the fused signal being able to approximate the real position closely, being able to approximate the direction of movement as well as an approximation of the velocity of the UMR. In P3, P4, P5, and P6 the interruptions are longer. Here the fused signal is still able to provide an approximation of the velocity, and it also shows changes in directions visible clearly at, for example, $t = 0.5$ s in (P5, M2)

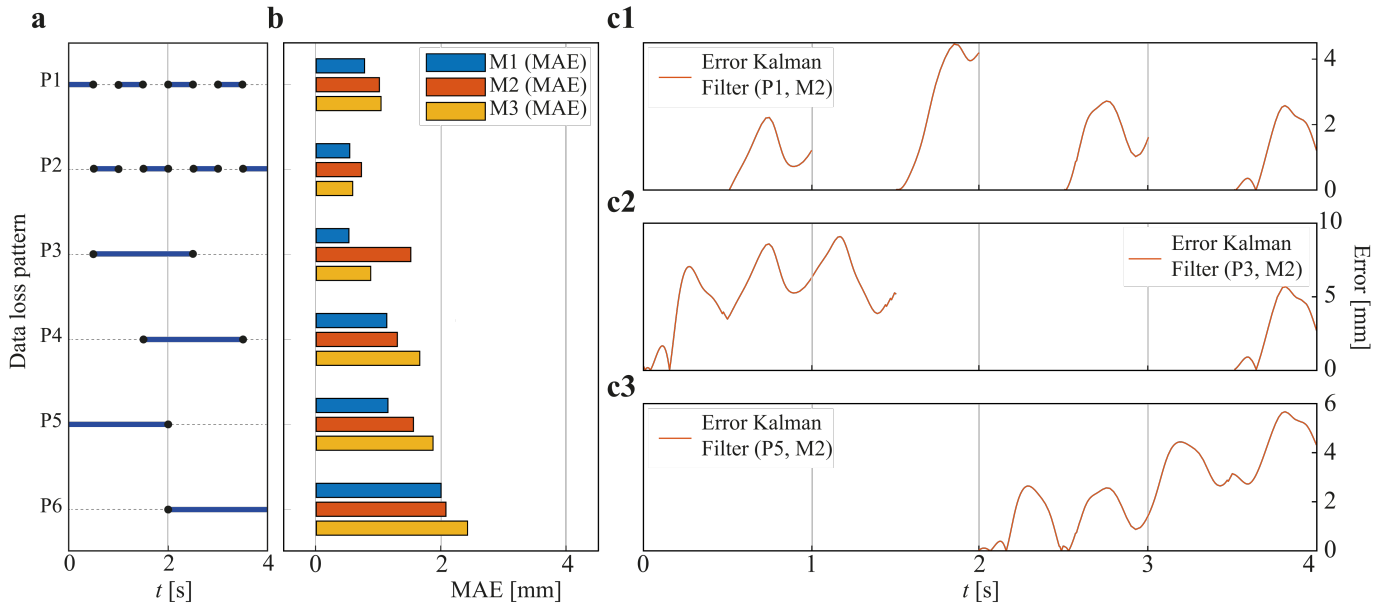

Fig. 11. Six distinct interruption patterns (P1-P6) are applied to 3 different measurements (M1-M3) resulting in 18 different trials. These interruption patterns simulate a loss in localization due to physical occlusion (e.g. bony material) or user error (e.g. lifting the transducer up and away from tissue or losing the UMR outside the field of view.) (a) The interruption patterns are indicated as a horizontal interrupted line for reference. (b) The mean absolute error (MAE) of the fused localization compared to the real position can be seen as a bar graph for each measurement and pattern combination. (c1) The mean error over time of (P1, M2) grows as time passes but is reset often by periods where the US localization is available. (c2-3) (P3, M2) shows, like (P5, M2), that the error grows more due to the longer interruption. This is reflected in the higher maxima in these trials.

and at $t = 2.5$ s in (P6, M2). The longer interruption patterns also show that for longer interruptions the error has more time to build up before being reset to zero by US localization. This increase in error is also reflected in the Mean Absolute Error (MAE) of those trials. The individual MAEs of each trial can be seen in Fig. 11(b). The error of the fused signal over time, evaluated just at the moments where US is interrupted, can be seen in Fig. 11(c1-3). (c1) shows the shorter interruptions of P1 and (c2-3) show a much longer build-up in error for the longer interruptions of patterns P3 and P5. In line with what visual inspection of the performance led us to believe, during longer interruptions (P3-P6) the MAE in Fig. 11(b) is higher, at 1.7 ± 0.4 mm compared to shorter interruptions where the mean MAE of P1 and P2 is 0.9 ± 0.2 mm. The combined MAE for all 18 trials is 1.4 ± 0.3 mm. The error dynamics show clearly that the error builds up over time and is reset when US localization comes back. During longer bouts of interruption the error is allowed to build up more, resulting in a higher error maximum. This behavior can be seen in Figs. 11(c1-3). Even with this error, this method still provides use, as it enables you to, in real time, ascertain an approximation of the position, its velocity, and directional changes of the UMR.

VII. Discussions

A. Challenges and Potential of MCL

Magnetic coupling between an RPM and a nearby UMR applies a disturbance torque on the rotor of the DC motor. Its motion due to this coupling induces a back-emf which would counteract the applied voltage during the actuation of the RPM, resulting in a change in the applied current. The effect of such magnetic coupling can be seen and obtained by measuring the current drawn and the angular velocity, during wireless actuation. We observe that the current and angular velocity are oscillatory with an exponentially increasing amplitude, while the estimated magnetic coupling increases monotonically as the localization gap decreases. This relation is also known accurately along the dipole axis of the RPM, allowing us to estimate the location of the UMR during wireless actuation. This localization method has the potential to determine the location of any UMR using the same signals that are used for actuation, allowing wireless manipulation systems to operate with much less dependence on medical imaging systems and magnetic field sensors. However, there exist at least three distinct challenges that must be addressed: 1) trade-offs between robust motion control and localization rate, 2) trade-offs between the localization gap and the step-out frequency of the UMR, and 3) down-scaling of the UMR.

The first challenge can be intuitively understood by considering a motion applied to the RPM actuator. This motion will induce back-emf and counteract the applied voltage, allowing a change in the current drawn. If the change in current is large enough, then the torque that caused the motion would be detectable. This means that an RPM in a speed control mode cannot maintain a desired angular velocity with relatively small steady-state error while simultaneously allowing for detectable motion by the UMR.

The second challenge is in the relationship between the step-out frequency and the localization gap. Associated with the increase in this gap is a decrease in the magnetic field at the position of the UMR and a decrease in its step-out frequency (e.g., Fig. 7(c) for $\Omega = 4$ Hz). This implies that when the localization gap is large, UMRs can be simultaneously actu-

ated and localized within a small frequency range below step-out frequency and above the zero dB crossing. Additionally, we note that the MAE displays an increasing trend as the localization gap decreases. This behavior is attributed to the increased field-gradient pulling that intensifies as the RPM approaches the lumen, consequently amplifying the friction torque on the RPM actuator.

The third challenge is the continuous demand for miniaturization to a scale relevant to clinical use. For a given localization gap, $\mathbf{p}$, and RPM magnetic moment, $\mathbf{M}$, the magnetic torque scales as $\|\mathbf{T}_{\mathrm{M}}\| \sim \|\mathbf{m}\|$ on the vertical axis between the RPM and the UMR (Fig. 3(b)). The magnetic moment is proportional to the UMR's volume [36]. Therefore, scaling the volume of the UMR with a factor s will change the magnetic moment of the UMR to $s^3\|\mathbf{m}\|$. This relationship implies that, for a given localization gap and RPM's magnetic moment, downscaling the UMR with a factor s causes the magnetic coupling to scale as $\|\mathbf{T}_{\mathrm{M}}\| \sim s^3\|\mathbf{m}\|$. To satisfy this requirement and produce detectable torque on the RPM actuator, the localization gap can be decreased resulting in strict constraint for relatively small UMRs.

Despite these many trade-offs, we have demonstrated that MCL is possible without any additional measurements and hardware. This implies that the motion control authority of the permanent-magnet robotic systems can be significantly improved. Naturally, the constraints and hardware collisions associated with the use of multiple robots for simultaneous actuation and localization are avoided. In addition, the workspace is kept unobstructed, providing a relatively large actuation workspace that is limited by the robotic arm.

B. Hybrid UMR Localization: Fusing MCL with Ultrasound Imaging

Fig. 7 illustrates that MCL works best within certain ranges of localization gaps and actuation speeds. Even though there is some control of these parameters in real-world situations, such applications will not always allow for setting parameters to optimal ranges, resulting in poorer MCL performance compared to the results seen in Section IV. In settings closer to in vivo experiments, challenges may arise. One issue might be the geometry of a patient imposing constraints on the region in which the RPM can operate, effectively imposing constraints on localization gaps. Another constraint could be due to blood flow inside a lumen counteracting the locomotion of the UMR, requiring higher actuation speeds, which could be outside optimal ranges for best localization.

When operating outside the ideal parameter ranges, there is a degradation of localization accuracy in the MCL-US fusion. Practically, this results in a faster accumulation of localization error when ultrasound is interrupted. While an increase in error accumulation is undesirable, the fused signal would still be continuous and provide information about changes in direction until US localization is restored. This means that even in sub-par situations, the fused signal is still an improvement compared to solely relying on US localization.

Fusion of MCL with US localization provides a way to get an uninterruptible, low latency localization, with increased sampling frequency compared to just US imaging-based localization, which is limited to a frequency of 20 Hz. With our implementation of US-MCL fusion, this frequency is increased to the sampling rate of MCL, at 167 Hz. With more efficient implementations in low-level coding languages, this frequency could be increased even more. This could solve one of the issues on the way to closed-loop control of the UMR's position. If adequate actuation speeds are to be achieved, the whole system needs to run with low latency consistently. Additionally, a low-pass filter could be used on the fused signal. This would decrease spikes in velocity, which would enable the use of a derivative term in a PD-control system.

VIII. Conclusions

In this work, we present the basic physical framework necessary to implement a noninvasive permanent MCL of UMRs actuated using a single RPM during 1-D motion in confined environments. Based on a magnetic coupling observer, we show both theoretically and experimentally that the error between the actual and estimated magnetic coupling between the RPM actuator and a UMR can be made arbitrarily small by increasing the cut-off frequency of the observer and operating at low actuation frequencies, allowing the position of the UMR to be estimated using a quadratic least-squares problem. We demonstrate simultaneous open-loop actuation and localization of a 12-mm magnetic roller at a 200-mm distance from the RPM actuator and achieve MAE of 0.7 ± 0.5 mm. Our measurements show that the MAE of the MCL method remains arbitrarily small (less than half-body-length) when it is actuated at frequencies slightly greater than the zero dB crossing of the actuator magnet, which can be positioned at localization gap that is many body lengths (less than 16 body lengths) further away from the UMR. Furthermore, we present successful localization of sub-centimeter-sized UMRs. Our measurements reveal that a 3-mm UMR can be localized with an MAE of 0.3 ± 0.1 mm at a localization gap of 180 mm.

We also implement a hybrid approach using data fusion to combine ultrasound localization and magnetic coupling localization through Kalman Filtering. This results in a more accurate and robust localization compared to each method individually, which would be critical during an operation with a UMR. Bones, soft tissue, and air are transparent to magnetic fields, which allows MCL to operate when the ultrasound imaging is obstructed by potential bony material or air pockets. At a 140 mm localization gap, with an actuation frequency of 1 Hz, we achieved an MAE of 1.4 ± 0.3 mm. The fusion of signals allows for continuous localization at the sampling frequency of MCL, which is 167 Hz. This uninterrupted localization enables closed-loop control, with the higher sampling rate enabling faster actuation of the UMR. The traditional method, solely using US imaging, would yield a non-continuous signal with a much lower sampling rate, at about 20 Hz. Since MCL uses a low-frequency magnetic field, its interaction with tissue is negligible. Therefore, its biocompatibility is comparable with that of pulse-echo and optical techniques. Finally, since MCL works without the

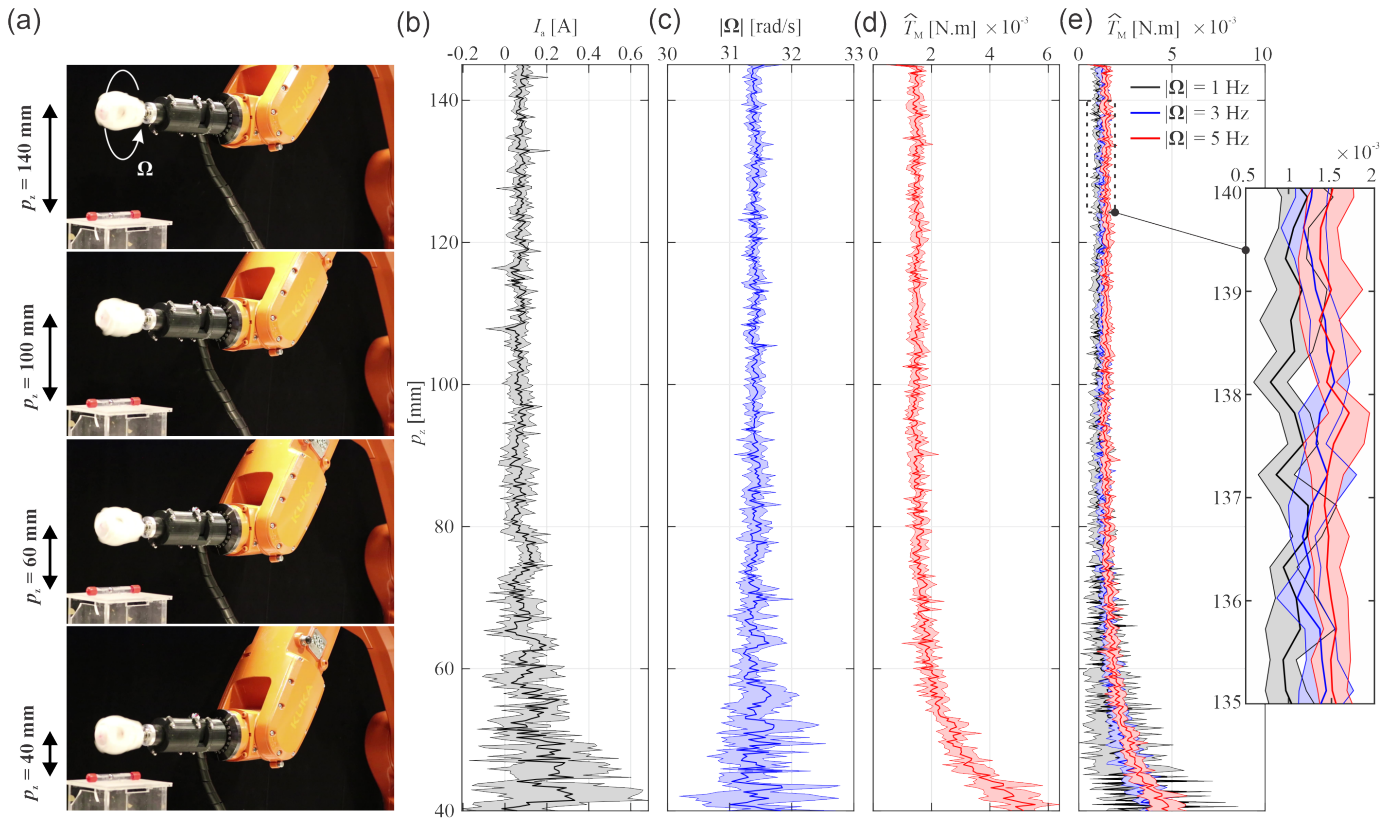

Fig. 12. Estimation of the magnetic coupling between the rotating permanent magnet (RPM) and a roller (12 mm) is implemented by moving the end-effector vertically, $\mathbf{p} = [0, 0, p_z]^T$. The RPM is an axially magnetized NdFeB disk with a diameter of 35 mm and a height of 20 mm. The angular velocity of the RPM is set to 31 rad/s. The experiment is repeated 5 times to determine the mean current, angular velocity, and magnetic coupling. The shading represents the standard deviation of the signals. a) The end-effector is allowed to move 10 cm along the $\mathbf{z}$-axis and the RPM's rotation axis is fixed at $\mathbf{\Omega}_{\text{act}} = |\mathbf{\Omega}|[1, 0, 0]^T$. b) The current increases with the decreasing distance between the RPM and the UMR. c) The amplitude of the angular velocity of the DC motor increases with the decreasing distance. d) The estimated disturbance torque increases approximately as the cube of the distance. e) Magnetic coupling is estimated at three angular velocities of the RPM ($|\mathbf{\Omega}| = 1, 3, 5$ Hz). The inset shows that the magnetic torque is amplified as the actuation is beyond the zero dB crossing [46].

need for sensors aboard the UMR or within the UMR's workspace, it is economically advantageous and works without any additional hardware.

For future work, it would be useful to characterize the error dynamics of fusion during longer bouts of interruption. This could inform expansions or changes to the method to improve the performance. Another area for future research is further exploration of MCL in 2D and 3D. This would open up the method to more widespread applications.

APPENDIX A

The amplitude and phase characteristics of the controlled RPM actuator depend on a PI/low-pass filter control system, $C(s) = (k_{\text{p}}s + k_{\text{i}})/s$, and the electrical transfer function of the motor, $E(s) = 1/(Ls + R)$, and the mechanical transfer function, $G(s) = 1/((J_1 + J_2)s + B)$, where k_{p} and k_{i} are the proportional and integral gains, respectively. It can be shown that the sensitivity, $|\Omega|/|\Omega_{\text{des}}|$, and tracking performance, $|\Omega|/|T_{\text{M}}|$, of the RPM actuator are given by

$$|\Omega|/|\Omega_{\text{des}}| = \frac{C(s)E(s)G(s)}{1 + C(s)E(s)G(s) + k_{\text{e}}E(s)G(s)}$$
$$|\Omega|/|T_{\text{M}}| = \frac{G(s)}{1 + C(s)E(s)G(s) + k_{\text{e}}E(s)G(s)}. \quad (29)$$

Explicit representations of the transfer functions in Equation (29) can be shown using the nominal parameters in Table II to determine the amplitude and phase characteristics in Figs. 4(a) and 4(b).

APPENDIX B

Experimental results demonstrating the torque estimation of the UMR are conducted using a KUKA KR-1100-2 6-DOF serial manipulator (Fig. 12(a)). This manipulator controls the pose of a Maxon 18 V brushless DC motor with integrated Hall-effect sensors, an encoder, and a planetary gearbox with a gear ratio of 3.7:1. A cylinder of NdFeB permanent magnet (Grade-N52) with a magnetic moment of 18.89 A.m^2 is attached to the motor to control the rotation of the magnetic field. The UMR is a 12 mm roller permanent magnet of NdFeB (Grade-N42) and a magnetic moment of 1.12 A.m^2. The UMR is contained within a transparent lumen with an inner diameter of approximately 15 mm. The lumen is filled with silicone oil with a viscosity of 1 Pa.s and the displacement of the UMR can be constrained enabling pure rotational motion and no translation. The lumen and the fluid allow us to visually track the UMR during the localization for validation. Figs. 12(b) and 12(c) show the measured current

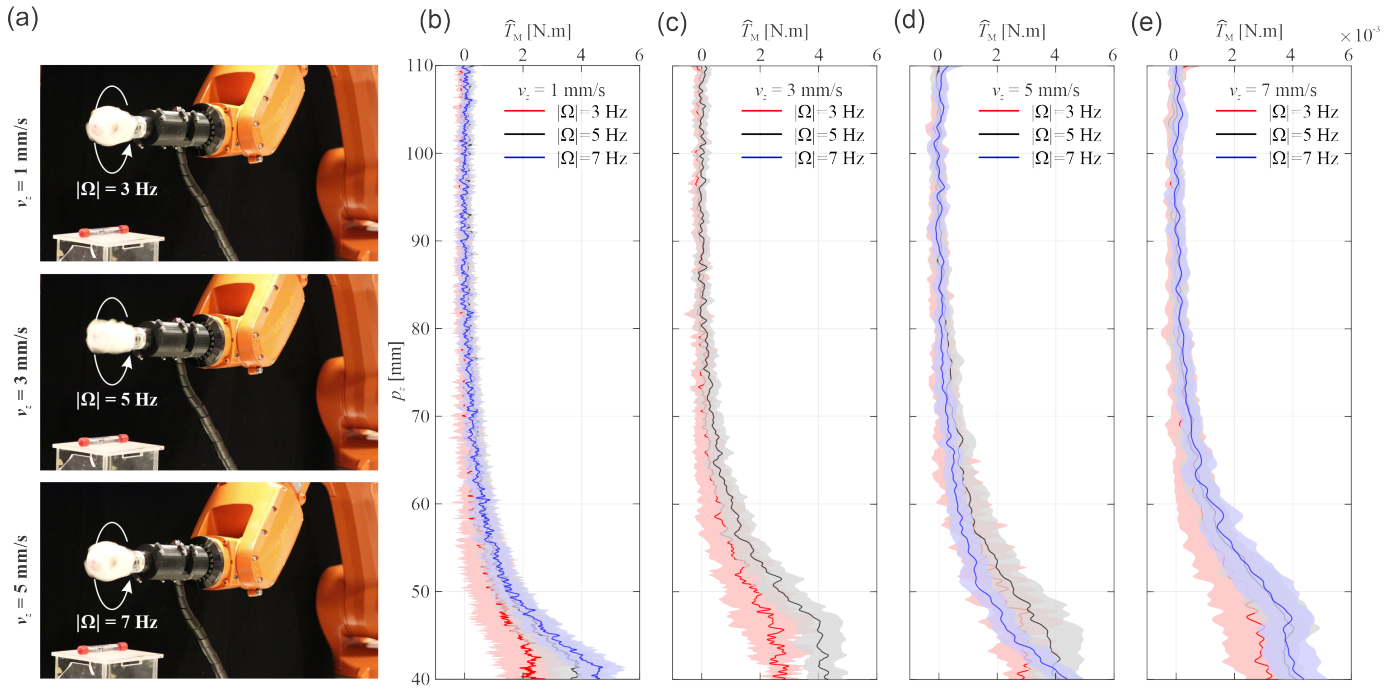

Fig. 13. Magnetic coupling estimation is achieved for various angular velocities, $\|\Omega\|$, of the rotating permanent magnet (RPM) and translational speeds, v_z, of the end-effector toward a 12 mm roller. The end-effector is controlled to move with translational motion $\mathbf{p} = [0, 0, p_z]^T$ and orientation of $\mathbf{\Omega}_{\text{act}} = |\mathbf{\Omega}|[0, 1, 0]^T$. The shading represents the standard deviation and the solid lines represent the average magnetic coupling ($n = 5$). a) The translational velocity of the RPM is controlled during the vertical motion toward the robot and its orientation is fixed. b) $v_z = 1$ mm/s and $|\mathbf{\Omega}| = 3, 5, 7$ Hz. c) $v_z = 3$ mm/s and $|\mathbf{\Omega}| = 3, 5, 7$ Hz. d) $v_z = 5$ mm/s and $|\mathbf{\Omega}| = 3, 5, 7$ Hz. e) $v_z = 7$ mm/s and $|\mathbf{\Omega}| = 3, 5, 7$ Hz [46].

and angular velocity, respectively, and the estimated magnetic coupling between the RPM and 12 mm UMR (Fig. 12(d)). In this experiment, the RPM is allowed to rotate at an angular velocity of approximately 31.5 rad/s in speed control mode (see Appendix A). The displacement of the RPM is controlled such that its rotational axis is parallel to the longitudinal axis of the fluid-filled lumen which contains the UMR (i.e., $\mathbf{\Omega}_{\text{act}} = |\mathbf{\Omega}|[1, 0, 0]^T$). This magnetic coupling allows the robot to rotate in sync with the RPM at a fixed location because of the physical constraint of the inner wall of the tube. The RPM is moved gradually toward the UMR at a translational speed of 1 mm/s within a range of 100 mm. The minimum distance between the RPM and the UMR is set to 40 mm as this is the minimum distance before the RPM collides with the lumen containing the UMR.

Vertical runs (i.e., $\mathbf{p} = [0, 0, p_z]^T$) of the RPM toward the UMR are repeated ($n = 5$) and the current and angular velocity are directly measured to estimate the magnetic coupling in real-time. Fig. 12(b) shows that the current increases with the distance between the RPM and the UMR. At a relatively large localization gap ($p_z = 140$ mm), the current drawn by the motor is 0.08 ± 0.02 A ($n = 5$). Accordingly, the rotational speed of the RPM varies between 31 ± 0.5 rad/s (Fig. 12(c)) for the relative distance range of $90 \leq p_z < 140$ mm. Note that the shading represents the standard deviation (s.d.) which is calculated for consecutive runs. There is no noticeable difference in current or angular velocity as the RPM moves closer to the UMR. However, for $p < 100$ mm the magnetic coupling is sufficient to trigger a noticeable increase in the current drawn and the associated angular velocity. At $p_z = 60$ mm, for example, the current drawn is measured as 0.15 ± 0.02 A and the angular velocity is 31.75 ± 1 rad/s, resulting in a measured magnetic coupling of $(2 \pm 0.3) \times 10^{-3}$ N.m.

The estimated magnetic coupling in Fig. 12(d) illustrates an inverse relation between the estimated torque and the relative distance between the RPM and the UMR. The governing equation (4) shows that the magnetic torque falls off as the inverse cube of the relative distance p_z. Therefore, the magnetic coupling observer (11) captures the theoretical behavior predicted by the model (4) and the inverse nonlinear relation between T_{M} and p_z. From Fig. 12(d) it is clear that associated with the decrease in the relative distance p_z is a noticeable increase in the estimated magnetic coupling.

Typical wireless actuation experiments involve a range of frequencies to obtain different locomotion velocities. We repeat the magnetic coupling measurements for three angular velocities of the RPM to examine the behavior of the magnetic coupling observer for the same nominal parameters and gains. Fig. 12(e) illustrates the estimated magnetic coupling for angular velocities of 1-5 Hz. This experiment indicates that the estimated magnetic coupling is independent of the angular velocity of the RPM on average. However, the estimation error increases with the actuation frequency (Fig. 4(c)), introducing undesirable localization error. The standard deviation (shading) of the estimated magnetic coupling at $\omega = 1$ Hz is much greater than that at $\omega = 3$ and $\omega = 5$ Hz. Note that the speed of the translational motion of the RPM with respect to the UMR can be simultaneously changed during the estimation of the magnetic torque. Fig. 13 shows the estimated magnetic

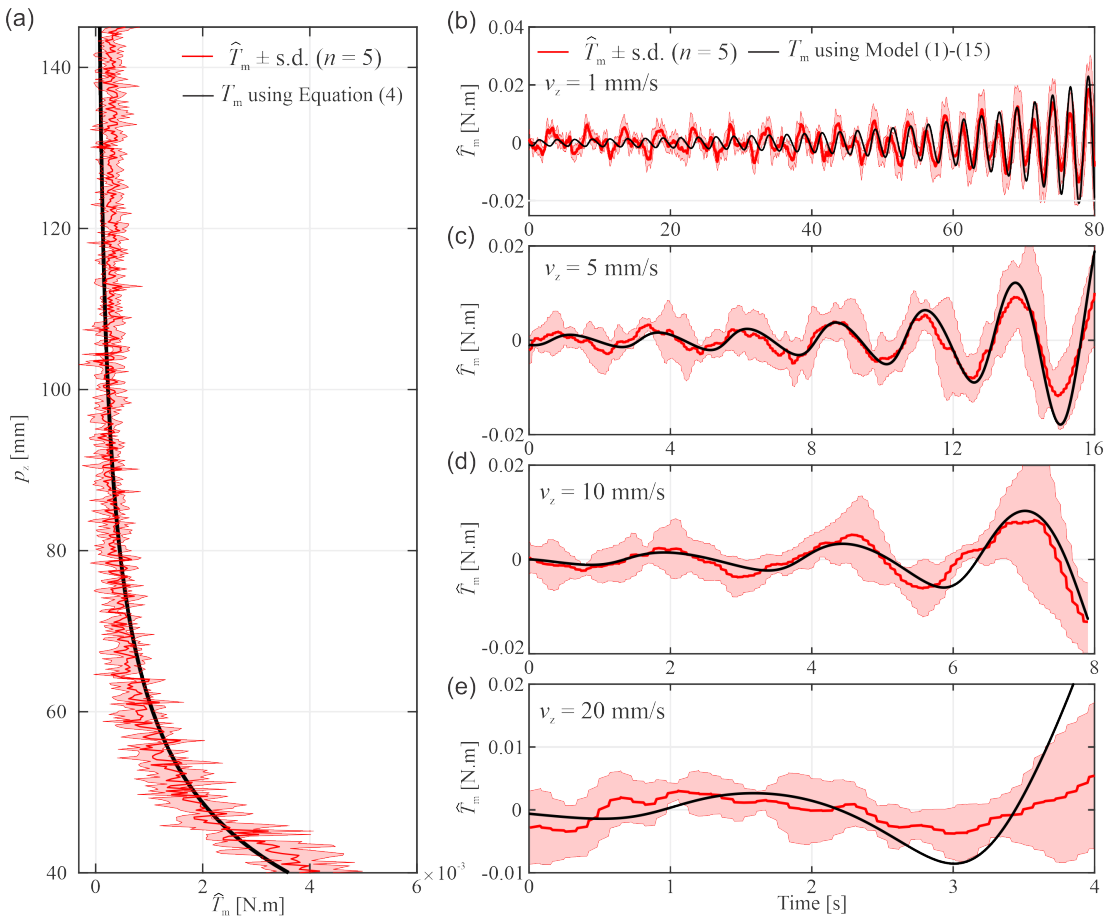

Fig. 14. The localization gap, p_z, between the rotating permanent magnet (RPM) and the UMR is decreased and the magnetic coupling, $T_{\rm m}$, is estimated. a) Magnetic coupling is predicted using Equation (4) and estimated using Equations (5) and (9). The standard deviation (s.d.) is calculated using 5 trials. b)-e) The estimated magnetic coupling based on the measured RPM's current and velocity is in agreement with the result of the model using equations (1)-(31). The amplitude of the magnetic coupling increases with the decreasing gap [46].

torque while the RPM rotates and translates at various speeds. In this experiment, the RPM is allowed to translate between $\mathbf{p} = [0, 0, 110]^T$ mm and $\mathbf{p} = [0, 0, 40]^T$ mm at translational speeds in the $1 \leq v_z \leq 7$ mm/s range. As the RPM moves toward the UMR at a higher speed the estimated magnetic torque increases at a much higher rate, as shown in Figs. 13(b)-13(e). With this dependence between the estimated magnetic torque and localization gap, the UMR can be localized by exploiting Equation (4).

Fig. 14(a) shows the estimated magnetic coupling between the RPM and the UMR for multiple vertical runs ($n = 5$). The minimum localization gap is set to 40 mm, and the RPM is allowed to rotate toward the UMR at a translational speed of $\sim$1 mm/s, while rotating about $\mathbf{\Omega}_{\rm act}$ at 3 Hz. The torque model (4) predicts that the magnetic coupling between the RPM and the UMR increases as the cube of the gap (black line), using the nominal values in Table II. The estimated magnetic coupling captures the behavior predicted by the model. Note that the deviation between the estimated magnetic coupling and the predicted values of the model is less than approximately $(3.9 \pm 1.6) \times 10^{-4}$ N.m for $p_z > 100$ mm. This deviation is attributed to error in the nominal geometric and magnetic parameters entered into the model and the observer. With the exception of this region ($p_z > 100$ mm), the magnetic coupling observer captures the behavior predicted by the theoretical model. For $40 < p_z \leq 100$ mm, the mean absolute error (MAE) between the estimated magnetic coupling and the results of the theoretical model is $(2.6 \pm 1) \times 10^{-4}$ N.m ($n = 5$).

The results of the magnetic model developed above (see Appendix B) between the UMR and the RPM (Fig. 5) are compared to the estimated magnetic coupling based on the RPM's current and angular velocity. Similarly, the translational motion of the RPM with respect to the UMR along the z-axis is provided at various speeds, as shown in Fig. 14(b)-14(e). In this experiment the magnetic coupling is estimated for $1 \leq v_z \leq 20$ mm/s and $125 \leq p_z \leq 40$ mm while rotation about $\Omega_{\rm act}$ at 1.25 rad/s. The MAE between the results of the theoretical model and the estimated mean magnetic coupling is 2.8 ± 2.6 mN.m.

APPENDIX C

The dynamics of the UMD with radius r is given by balance between magnetic, drag, and contact force, $\mathbf{f}_{\rm c}$, and torque, $\mathbf{T}_{\rm c}$, as [42]

$$\begin{aligned} \mathbf{f}_{\rm m} + 6\pi\eta r \left(f_{\rm t} \dot{\mathbf{p}} + f_{\rm r} r \boldsymbol{\omega} \right) + \mathbf{f}_{\rm c} = 0 \\ \mathbf{T}_{\rm m} + 8\pi\eta r^2 \left(T_{\rm t} \dot{\mathbf{p}} + T_{\rm r} r \boldsymbol{\omega} \right) + \mathbf{T}_{\rm c} = 0, \end{aligned} \tag{30}$$

where f_{t} and f_{r} are normalized scalar near-wall fluid forces of the translational and rotational motion, respectively, and T_{t} and T_{r} are their corresponding normalized scalar torques. The contact force and torque are given by

$$\mathbf{f}_{\mathrm{c}} = \mu_{\mathrm{f}} g \left(M - \frac{4}{3}\pi \rho_{\mathrm{m}} r^3 \right), \quad \text{and} \quad \mathbf{T}_{\mathrm{c}} = r\mathbb{N} \times \mathbf{f}_{\mathrm{c}}, \tag{31}$$

where μ_{f} is a dynamic coefficient of friction, g is the gravitational acceleration, $\mathbb{P}$ is a velocity vector of unit length, and $\mathbb{N}$ is a unit vector normal to the plane of motion. Equations (1)-(15) are used to determine the relationship between the magnetic coupling observer gain, g, and the error between the actual and estimated magnetic torque in Fig. 4(c).

REFERENCES

[1] B. J. Nelson, I. K. Kaliakatsos, and J. J. Abbott, "Microrobots for minimally invasive medicine," *Annual Review of Biomedical Engineering*, vol. 12, no. 1, pp. 55–85, Aug. 2010.

[2] M. Sitti, H. Ceylan, W. Hu, J. Giltinan, M. Turan, S. Yim, E. Diller, "Biomedical applications of untethered mobile milli/microrobots," *Proceedings of the IEEE*, vol. 103, no. 2, pp. 205-224, Feb. 2015.

[3] J. Wu, D. Folio, J. Zhu, B. Jang, X. Chen, J. Feng, P. Gambardella, J. Sort, J. Puigmartí-Luis, O. Ergeneman, A. Ferreira, S. Pané, "Motion analysis and real-time trajectory prediction of magnetically steerable catalytic janus micromotors," *Advanced Intelligent Systems*, vol. 4, no. 11, 2200192, Nov. 2022.

[4] A. Aziz, S. Pane, V. Iacovacci, N. Koukourakis, J. Czarske, A. Menciassi, M. M. Sánchez, and O. G. Schmidt, "Medical imaging of microrobots: Toward in vivo applications," *ACS Nano*, vol. 14, no. 9, pp. 10865-10893, Sep.2020.

[5] F. Bianchi, A. Masaracchia, E. S. Barjuei, A. Menciassi, A. Arezzo, A. Koulaouzidis, D. Stoyanov, P. Dario, and G. Ciuti, "Localization strategies for robotic endoscopic capsules: a review," *Expert Review of Medical Devices*, vol. 16, no. 5, pp. 381-403, May 2019.

[6] S. Pané, P. Wendel-Garcia, Y. Belce, X.-Z. Chen, J. Puigmartí-Luis, "Powering and fabrication of small-scale robotics systems," *Springer International Publishing*, vol. 2, pp. 427–440, Oct. 2021.

[7] R. Dreyfus, J. Baudry, M. L. Roper, M. Fermigier, H. A. Stone, and J. Bibette, "Microscopic artificial swimmers," *Nature*, 437, 862-865, October 2005.

[8] L. Zhang, J. J. Abbott, L. Dong, B. E. Kratochvil, D. Bell, and B. J. Nelson, "Artificial bacterial flagella: fabrication and magnetic control," *Applied Physics Letters*, vol. 94, no. 6, pp. 064107, February 2009.

[9] R. Pieters, H.-W. Tung, S. Charreyron, D. F. Sargent, and B. J. Nelson, "RodBot: a rolling microrobot for micromanipulation," in *IEEE International Conference on Robotics and Automation (ICRA)*, pp. 4042–4047, May 2015.

[10] Y. Alapan, U. Bozuyuk, P. Erkoc, A. C. Karacakol, and M. Sitti, "Multifunctional surface microrollers for targeted cargo delivery in physiological blood flow," *Science Robotics*, vol. 5, May 2020.

[11] J. J. Abbott, E. Diller, and A. J. Petruska, "Magnetic methods in robotics," *Annual Review of Control, Robotics, and Autonomous Systems*, 3:57–90, 2020.

[12] G. Pittiglio, M. Brockdorff, T. da Veiga, J. Davy, J. H. Chandler and P. Valdastri, "Collaborative magnetic manipulation via two robotically actuated permanent magnets," *IEEE Transactions on Robotics*, 2022, doi: 10.1109/TRO.2022.3209038.

[13] M. Vonthron, V. Lalande, G. Bringout, C. Tremblay, and S. Martel, "A MRI-based integrated platform for the navigation of microdevices and microrobots," in *Proc. IEEE J. Int. Conf. Intell. Robots Syst.*, San Francisco, CA, USA, Sep. 2011, pp. 1285–1290.

[14] M. E. Tiryaki, F. Dogangun, C. B. Dayan, P. Wrede, and M. Sitti, "MRI-powered magnetic miniature capsule robot with HIFU-controlled on-demand drug delivery," in *Proceedings of the IEEE International Conference on Robotics and Automation (ICRA)*, pp. 5420-5425, 2023.

[15] J. Edelmann, A. J. Petruska, Bradley J. Nelson, "Estimation-Based control of a magnetic endoscope without device localization ," *Journal of Medical Robotics Research*, 3:1850002, 2018.

[16] A. Hong, A. J. Petruska and B. J. Nelson, "Tracking a magnetically guided catheter with a single rotating C-Arm," in *Proceedings of the IEEE International Conference on Robotics and Automation (ICRA)*, Seattle, WA, pp. 618–623, 2015.

[17] J. B. Mathieu, G. Beaudoin, and S. Martel, "Method of propulsion of a ferromagnetic core in the cardiovascular system through magnetic gradients generated by an MRI System," *IEEE Trans. Biomed. Eng.*, vol. 53, pp. 29–299, 2006.

[18] I. S. M. Khalil, D. Mahdy, A. El Sharkawy, R. R. Moustafa, A. F. Tabak, M. Elwi, S. Hesham, N. Hamdi, A. Klingner, A. Mohamed, and M. Sitti, "Mechanical rubbing of blood clots using helical robots under ultrasound guidance," *IEEE Robotics Automation Letters (RAL)*, vol. 3, no. 2, pages 1112–1119, April 2018.

[19] L. V. Wang, J. Yao. A practical guide to photoacoustic tomography in the life sciences. Nat. Methods, 13, 627(2016).

[20] H. Daguerre, S. O. Demir, U. Culha, F. Marionnet, M. Gauthier, M. Sitti, and A. Bolopion, "A localization method for untethered small-scale robots using electrical impedance tomography," IEEE/ASME Transactions on Mechatronics, vol. 27, no. 5, pp. 3506-3516, Oct. 2022.

[21] A. Z. Taddese, P. R. Slawinski, M. Pirotta, E. De Momi, K. L. Obstein, and P. Valdastri, "Enhanced real-time pose estimation for closed-loop robotic manipulation of magnetically actuated capsule endoscopes," *The International Journal of Robotics Research*, vol. 37, no. 8, pp. 890-911, Jun. 2018.

[22] X. Yan, Q. Zhou, M. Vincent, Y. Deng, J. Yu, J. Xu, T. Xu, T. Tang, L. Bian, Y.-X. J. Wang, K. Kostarelos, and Li Zhang, "Multifunctional biohybrid magnetite microrobots for imaging-guided therapy," *Science Robotics*, vol. 2, no. 12, Nov. 2017.

[23] Q. Wang, L. Yang, J. Yu, P. W. Y. Chiu, Y.-P. Zheng, and L. Zhang, "Real-Time magnetic navigation of a rotating colloidal microswarm under ultrasound guidance," *IEEE Trans. Biomed. Eng.*, vol. 67, no. 12, Dec. 2020.

[24] C. Di Natali, M. Beccani, and P. Valdastri, "Real-Time pose detection for magnetic medical devices," *IEEE Trans. Magn.*, 49(7), 3524–3527, 2013.

[25] E. E. Niedert, C. Bi, G. Adam, E. Lambert, L. Solorio, C. J. Goergen, and D. J. Cappelleri, "A tumbling magnetic microrobot system for biomedical applications," *Micromachines*, vol. 11, no. 9, Sep. 2020.

[26] Servant, F. Qiu, M. Mazza, K. Kostarelos, and B. J. Nelson, "Controlled in vivo swimming of a swarm of bacteria-like microrobotic flagella," Adv.Mater., vol. 27, no. 19, pp. 2981–2988, Apr. 2015.

[27] S. Pane, G. Faoro, E. Sinibaldi, V. Iacovacci, and A. Menciassi, "Ultrasound acoustic phase analysis enables robotic visual-servoing of magnetic microrobots," *IEEE Transactions on Robotics,* vol. 38, no. 3, pp. 1571-1582, June 2022.

[28] K. M. Popek, T. Hermans, and J. J. Abbott, "First demonstration of simultaneous localization and propulsion of a magnetic capsule in a lumen using a single rotating magnet," in *Proc. IEEE Int. Conf. Robot. Autom.*, pp. 1154–1160, 2017.

[29] K. M. Miller, A. W. Mahoney, T. Schmid, and J. J. Abbott, "Proprioceptive magnetic-field sensing for closed-loop control of magnetic capsule endoscopes," in *IEEE/RSJ Int. Conf. Intell. Robots Syst.*, 2012, pp. 1994–1999.

[30] C. Hu, M. Li, S. Song, W. Yang, R. Zhang and M. Q. Meng, "A Cubic 3-Axis Magnetic Sensor Array for Wirelessly Tracking Magnet Position and Orientation," *IEEE Sensors Journal*, vol. 10, no. 5, pp. 903–913, May 2010.

[31] S. Song , Li B, Qiao W, et al, "6-D magnetic localization and orientation method for an annular magnet based on a closed-form analytical model, "*IEEE Trans. Magn.*, 50(9), 1–11, 2014.

[32] D. Son, S. Yim, and M. Sitti, "A 5-D localization method for a magnetically manipulated untethered robot using a 2-D array of Hall-effect sensors," *IEEE/ASME Trans. Mechatronics*, vol. 21, no. 2, 2016.

[33] D. Son, S. Yim, and M. Sitti, "A 5-D localization method for a magnetically manipulated untethered robot using a 2-D array of Hall-effect sensors," *IEEE/ASME Trans. Mechatronics*, vol. 21, no. 2, 2016.

[34] M. Zhang, L. Yang, C. Zhang, Z. Yang, and L. Zhang, "A 5-D large-workspace magnetic localization and actuation system based on an eye-in-hand magnetic sensor array and mobile coils," *IEEE Transactions on Instrumentation and Measurement*, vol. 72, 2023.

[35] A. W. Mahoney and J. J. Abbott, "Managing magnetic force applied to a magnetic device by a rotating dipole field," *Applied Physics Letters*, vol. 99, no. 13, pp. 134-103, Sep. 2011.

[36] A. W. Mahoney and J. J. Abbott, "Generating rotating magnetic fields with a single permanent magnet for propulsion of untethered magnetic devices in a lumen," *IEEE Transactions on Robotics,* vol. 30, no. 2, pp. 411-420, Apr. 2014.

[37] A. W. Mahoney and Jake J. Abbott, "Five-degree-of-freedom manipulation of an untethered magnetic device in fluid using a single permanent magnet with application in stomach capsule endoscopy," *the*

International Journal of Robotics Research, vol. 35, no. 1-3, pp. 129–147, 2016.

[38] S. Katsura and K. Ohnishi, "Force Servoing by Flexible Manipulator Based on Resonance Ratio Control," *IEEE Transactions on Industrial Electronics*, vol. 54, no. 1, pp. 539-547, Feb. 2007.

[39] K. Ohishi, K. Ohnishi, and K. Miyachi, "The torque regulator using the observer of dc motor. In *Report of IEE of Japan*, pap. RN–82–33, 1982.

[40] W.-H Chen, J. Yang, L. Guo, and S. Li, "Disturbance observer based control and related methods: an overview," *IEEE Transactions on Industrial Electronics,* Vol. 63, No. 2, pp.1083-1095, 2016.

[41] W.-H. Chen, "Disturbance observer based control for nonlinear systems," *IEEE/ASME Transactions on Mechatronics*, vol. 9, no. 4, pp. 706-710, Dec. 2004.

[42] M. M. Micheal, A. Adel, C.-S. Kim, J.-oh Park, S. Misra, and I. S. M. Khalil, "2D magnetic actuation and localization of a surface milli-roller in low Reynolds numbers," *IEEE Robotics and Automation Letters*, Jan. 2022.

[43] J. Snyder, Y. Silverman, Y. Bai, and M. A. MacIver, "Underwater object tracking using electrical impedance tomography," in *Proc. IEEE/RSJ Int. Conf. Intell. Robots Syst.*, Oct. 2012, pp. 520–525.

[44] T. W. R. Fountain, Prem V. Kailat, and J. J. Abbott, "Wireless control of magnetic helical microrobots using a rotating-permanent-magnet manipulator," in *Proc. IEEE Int. Conf. Robot. Autom.*, 2011, pp. 576–581.

[45] Xiangheng Liu, and A. Goldsmith, "Kalman filtering with partial observation losses," in *43rd IEEE Conference on Decision and Control (CDC).*, 2004, pp. 4180-4186

[46] J. E. van Seeventer, "Observer-based Localization and Control of an Untethered Magnetic Microrobot," in *Essays Utwente, as part of a Bachelors' Thesis at the University of Twente in the department of Biomechanical Engineering, Faculty of Engineering Technology.*, 2022

[47] R. Avaneesh, "Actuation, Control and Localization of Untethered Magnetic Robots," in *Essays Utwente, as part of a Masters' Thesis at the University of Twente in the department of Biomechanical Engineering, Faculty of Engineering Technology.*, 2022